

The Central Kiloparsec of Seyfert and Inactive Host Galaxies: a Comparison of Two-Dimensional Stellar and Gaseous Kinematics.

Gaelle Dumas, Carole Mundell, Eric Emsellem, Neil Nagar

▶ **To cite this version:**

Gaelle Dumas, Carole Mundell, Eric Emsellem, Neil Nagar. The Central Kiloparsec of Seyfert and Inactive Host Galaxies: a Comparison of Two-Dimensional Stellar and Gaseous Kinematics.. Monthly Notices of the Royal Astronomical Society, 2007, 379 (4), pp.1249-1278. 10.1111/j.1365-2966.2007.12014.x . ensl-00137409

HAL Id: ensl-00137409

https://ens-lyon.hal.science/ensl-00137409

Submitted on 29 May 2007

HAL is a multi-disciplinary open access archive for the deposit and dissemination of scientific research documents, whether they are published or not. The documents may come from teaching and research institutions in France or abroad, or from public or private research centers.

L'archive ouverte pluridisciplinaire **HAL**, est destinée au dépôt et à la diffusion de documents scientifiques de niveau recherche, publiés ou non, émanant des établissements d'enseignement et de recherche français ou étrangers, des laboratoires publics ou privés.

Mon. Not. R. Astron. Soc. **000**, 1–32 (...) Printed 29 May 2007 (MN LATEX style file v2.2)

The Central Kiloparsec of Seyfert and Inactive Host Galaxies: a Comparison of Two-Dimensional Stellar and Gaseous Kinematics.

Gaëlle Dumas[1,2⋆], Carole G. Mundell[2], Eric Emsellem[1], Neil M. Nagar[3]
[1] *Université de Lyon 1, CRAL, Observatoire de Lyon, 9 av. Charles André, F-69230 Saint-Genis Laval; CNRS, UMR 5574 ; ENS de Lyon, France.*
[2] *Astrophysics Research Institute, Liverpool John Moores University, Twelve Quays House, Egerton Wharf, Birkenhead CH41 1LD, UK.*
[3] *Astronomy Group, Universidad de Concepción, Concepción, Chile.*

Accepted ... Received ... in original ...

ensl-00137409, version 1 - 29 May 2007

ABSTRACT
We investigate the properties of the two-dimensional distribution and kinematics of ionised gas and stars in the central kiloparsecs of a matched sample of nearby active (Seyfert) and inactive galaxies, using the SAURON Integral Field Unit on the William Herschel Telescope. The ionised gas distributions show a range of low excitation regions such as star formation rings in Seyferts and inactive galaxies, and high excitation regions related to photoionisation by the AGN. The stellar kinematics of all galaxies in the sample show regular rotation patterns typical of disc-like systems, with kinematic axes which are well aligned with those derived from the outer photometry and which provide a reliable representation of the galactic line of nodes. After removal of the non-gravitational components due to e.g. AGN-driven outflows, the ionised gas kinematics in both the Seyfert and inactive galaxies are also dominated by rotation with global alignment between stars and gas in most galaxies. This result is consistent with previous findings from photometric studies that the large-scale light distribution of Seyfert hosts are similar to inactive hosts. However, fully exploiting the two-dimensional nature of our spectroscopic data, deviations from axisymmetric rotation in the gaseous velocity fields are identified that suggest the gaseous kinematics are more disturbed at small radii in the Seyfert galaxies compared with the inactive galaxies, providing a tentative link between nuclear gaseous streaming and nuclear activity.

Key words: galaxies: active - galaxies: spiral - galaxies: Seyfert - galaxies: kinematics and dynamics - galaxies: structure.

1 INTRODUCTION

It is now widely accepted that central supermassive black holes (SMBH) are ubiquitous in bulge-dominated galaxies (Ferrarese & Merritt 2000; Gebhardt et al. 2000), but ongoing nuclear activity is observed only in 10 to 20 per cent of nearby galaxies, 3 per cent at the Seyfert level (Kewley et al. 2006) suggesting black hole re-ignition via accretion of material in the central parts of the galaxy is required. A key unanswered question is whether the ignition mechanism is related to the galaxy host properties in particular the fuel transportation mechanism. Spiral galaxies contain a rich supply of potential fuel and the search for a mechanism to remove angular momentum and drive material towards the nucleus has been the focus of many studies. Numerical simulations predict efficient gas radial inflows due to non-axisymmetric perturbations in the gravitational potential such as bars or driven by galaxy interactions (Wada 2004), which may help to bring gas close to the galactic nucleus. However, most of past imaging studies failed to find any significant differences between galaxies hosting an Active Galactic Nucleus (AGN) or not, on spatial scales that encompass nearby companions/galactic interactions (De Robertis et al. 1998; Schmitt 2001; Ho et al. 2003), stellar bars or nuclear spirals (Mulchaey & Regan 1997; Laurikainen et al. 2004; Martini et al. 2003). In contrast, Hunt & Malkan (2004) conducted a NICMOS/HST imaging study of the circum-nuclear regions of 250 nearby galaxies and found a significant excess of isophotal twists in the circumnuclear regions of Seyfert 2 galaxies, compared to other categories (HII/Starburst, Seyfert 1, LINER, inactive galaxies). This result may hint at an evolutionary scenario to explain the

⋆ E-mail: gdumas:obs.univ-lyon1.fr (GD)

© ... RAS

different states in which a nearby galaxy is observed, and could suggest the presence of identifiable dynamical differences between Seyfert and inactive galaxies in the central kpc regions.

Probing the dynamics of Seyfert galaxies requires spectroscopic data. Single aperture and long-slit spectroscopy studies are clearly inadequate to investigate the complex structures observed in the central kpc of Seyfert galaxies. Two-dimensional spectroscopy (integral-field spectroscopy, IFS hereafter) is therefore a pre-requisite to study the dynamics of the gaseous and stellar components. Early work with such instruments provided two-dimensional gas and stellar kinematic maps of the central parts of a few nearby active galaxies, in optical wavelength: e.g. NGC 4151 (Mediavilla & Arribas 1995), NGC 3227 (Mediavilla & Arribas 1993), NGC 1068 (Garcia-Lorenzo et al. 1997) with INTEGRAL (an IFS based on optical fibers), or NGC 2110 (Ferruit et al. 2004) using OASIS (an IFS using a microlens array), as well as in the near infrared (NIR): The Circinus galaxy observed with the NACO spectrograph and SINFONI at the VLT (Prieto et al. 2004; Mueller Sánchez et al. 2006), NGC 3227 (Davies et al. 2006) observed with SINFONI. Multiple gaseous systems and kinematic perturbations are sometimes revealed, but the corresponding field-of-view (FOV) and/or the angular resolution were often too small to disentangle the AGN-related and galactic disc line emissions. Statistical conclusions cannot be drawn from these detailed studies of individual Seyfert galaxies, originally targeted for their complex nuclear properties and lacking any control inactive galaxy comparison. More recenly, the molecular gas in the central part of a larger (though still small) sample of Seyfert galaxies was observed using the Plateau de Bure Interferometer in the course of the NUGA survey (García-Burillo et al. 2003), revealing the potential role of gravity torques in the feeding of the inner 100 pc (e.g. García-Burillo et al. 2005). Gas reponds non-linearly to deviations from axisymmetry so a more direct link with the gravitational potential is still difficult to establish, due to the lack of large-scale stellar kinematic maps for these galaxies. Six nearby Seyferts were also observed with GMOS/Gemini, enabling the mapping of the ionised gas and stellar kinematics in the central few arcseconds (Barbosa et al. 2006). IFS such as SINFONI/VLT reached regions even closer to the nucleus (Davies et al. 2006), thanks to the use of adaptive optics. Again, such observations are useful for studying the kinematics in the nuclear regions, identifying the putative molecular torus around the SMBH, retrieving the characteristics of the central engine such as the mass of the SMBH, or studying the environment of the active nucleus. However, observed kinematics at these relatively small scales are rather difficult to interpret in the context of the host galaxy, considering the significant influence of non-gravitationally driven processes (e.g. outflows).

The SAURON IFS, mounted on the William Herschel Telescope (La Palma, Spain) has FOV ($33'' \times 41''$ in low resolution mode) that is large enough to observe ionised gas under the influence of the galaxy host potential, and a high enough spatial sampling to still probe the AGN-related emission in the inner parts. These data are then well suited to study both the stellar and gaseous kinematics in the above-mentioned context of fueling. A number of key studies were recently performed with SAURON providing unique datasets for a sample of nearby early-type (de Zeeuw et al. 2002; Emsellem et al. 2004; Sarzi et al. 2006) and spiral galaxies (Ganda et al. 2006; Falcón-Barroso et al. 2006). As a spin off, the distribution and kinematics of the gas and stellar components were also obtained and studied for some well known Seyfert (NGC 1068, Emsellem et al. 2006, NGC 5448, Fathi et al. 2005) or spiral inactive galaxies like M 100 (Allard et al. 2006). These works provided evidence for the existence of ionised gaseous inward streaming in the inner few kpc, hinting at a mechanism for transporting gas in the circumnuclear regions and further. However, no survey has been yet pursued to map the two-dimensional kinematic and morphology in the central parts of a well-selected sample of Seyfert and inactive galaxies, in order to search for and quantify potential dynamical differences between these two populations at these spatial scales.

We therefore designed a new IFS survey for a well-defined sample of active and control inactive galaxies, selected from the RSA sample with nuclear classification of Ho et al. (1997). This program aims at probing the galactic potential of the host galaxies by comparing the properties of both the ionised gas and stellar components in the circumnuclear regions of Seyfert galaxies. We observed these galaxies with the SAURON IFS, which provides a spatial coverage sufficient to map regions from the central $33'' \times 41'' \sim$ few kpc down to the inner $1'' \sim 50$ pc at 10 Mpc. In Sect. 2, we present the sample selection, the observations and data reduction. In Sect. 3, we present the associated stellar and ionised gas maps. A kinematic analysis is presented in Sect. 4. We then briefly discuss our results in a more general context and conclude in Sect. 5.

2 OBSERVATIONS AND ANALYSIS

2.1 Sample Selection

The observations presented here form part of a larger multi-wavelength campaign to investigate host galaxy structure and kinematics on size scales ever-closer to the nucleus, aimed at identifying or eliminating possible triggering and fueling mechanisms (Mundell 2003; García-Burillo et al. 2005). Our master sample consists of 39 Seyfert galaxies selected from the RSA catalogue paired with 39 control galaxies with carefully matched optical properties: B_T, Hubble type, inclination and, where possible, V_{sys} ($\leqslant 4000$ km s^{-1}). 3D spectroscopic imaging with the VLA and WSRT is underway to map the large-scale neutral hydrogen HI distribution and kinematics for these galaxies (Mundell et al. 2007). Current HI imaging interferometers however cannot routinely resolve structures smaller than $\sim 20''$ (i.e. $r < 700$ pc for our sample); studying the distribution and kinematics of ionised gas and stars with the integral-field spectrograph SAURON provides the missing link between the large-scale HI disc properties and the very central nuclear regions.

For our SAURON study, we selected a distance-limited sub-sample of Seyfert+control galaxies with $V_{sys} < 1600$ km s^{-1} to ensure that Fe stellar absorption lines lie well within the spectral band for the full SAURON field-of-view. Measurement of these Fe lines is critical in the presence of emission lines from ionised gas that contaminate Mg lines (see Sect. 2.3). In total, our sub-sample comprises 15

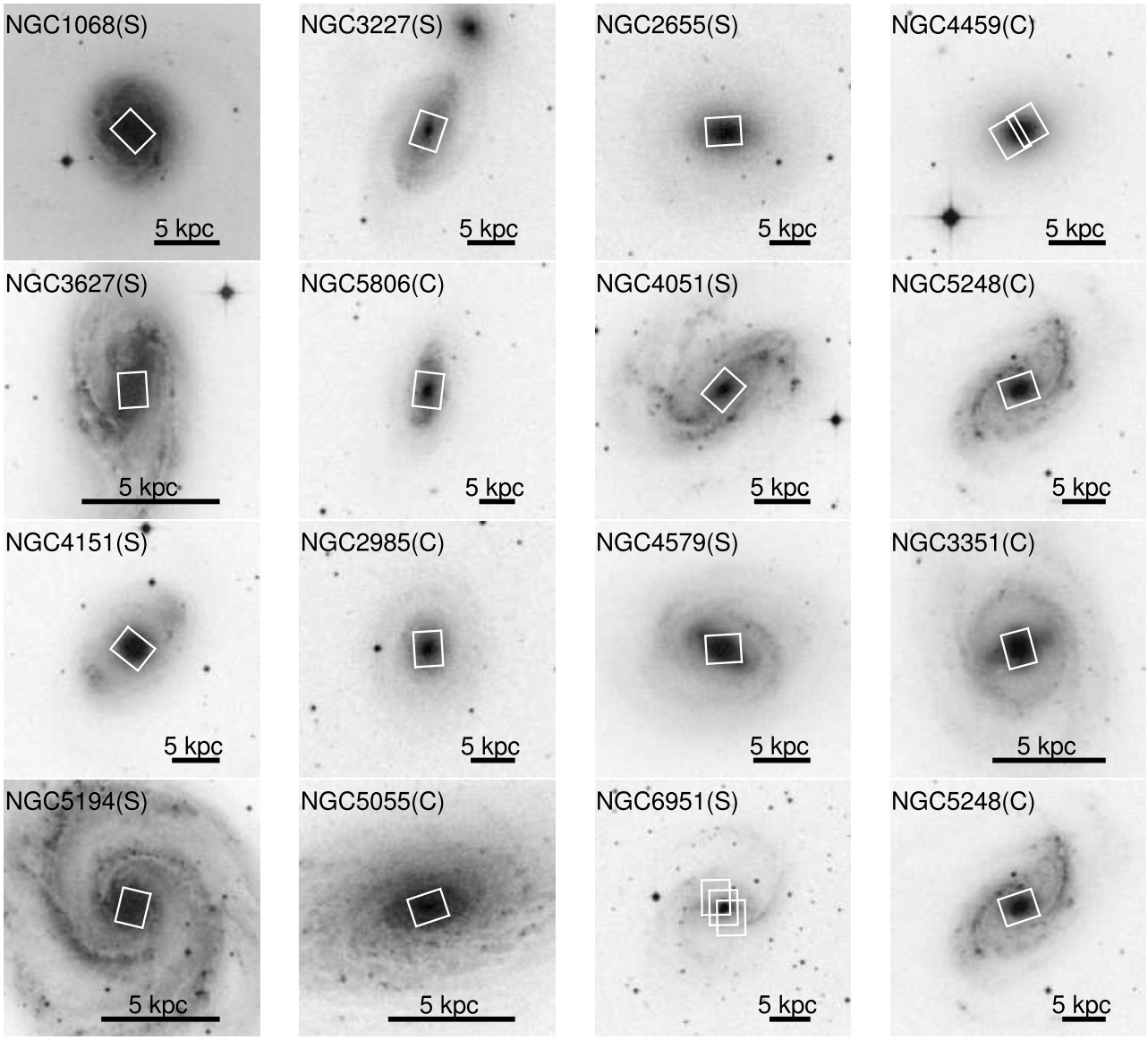


Figure 1. R-band Digital Sky Survey images of the sample galaxies. The '(S)' or '(C)' on the right of the object names stand for Seyfert or Control galaxy, respectively. Each Seyfert galaxy is displayed on the left of its associated control galaxy, except for NGC 1068 and NGC 3227 (first two panels) for which no control has been observed. The orientation is such that North is up and East is left, the bar located at the bottom right corner of each panel corresponds to the spatial length of 5 kpc. Overplotted on each image is the position of the SAURON field of view for that galaxy.

pairs of Seyferts+inactive galaxies. We completed observations of 7 pairs and two well-known Seyferts (NGC 1068 and NGC 3227) with no control galaxy data. NGC 1068 has been studied in detail by Emsellem et al. (2006) and is included here for completeness, while weather constraints prevented observations of the control galaxy for NGC 3227. Table 1 lists the properties of the sample galaxies. The V-band absolute magnitudes of the Seyfert nuclei in this sub-sample span the full magnitude range of the 25 brightest Seyfert nuclei in the RSA catalogue ($-20.9 < M_V < -16.0$), thus offering a representative selection of Seyfert activity.

2.2 SAURON Observation and Data Reduction

Observations of our sample were carried out between 2001 and 2004 using the integral-field spectrograph SAURON at the 4.2m William Herschel Telescope (WHT) at La Palma, Spain. Table 2 summarizes the exposure time for each pointing and lists the equivalent seeing of final reduced data.

The low spatial resolution mode of SAURON was used, providing a field-of-view (FOV) of $33'' \times 41''$ with a square sampling of 0.94 arcsec per spatial element (lens). This delivers about 1500 spectra simultaneously per object which cover the spectral range 4825-5380 Å, with a resolution of 4.2 Å. This wavelength range includes a number of important stellar absorption lines (Hβ, Fe5015, Mgb, Fe5270) and

Pairs	Name NGC	Type	T	Distance (Mpc)	D_{25} (arcmin)	Inclination (deg)	B_T (mag)	Vsys ($km\,s^{-1}$)	M_V(nuclear) (mag)	Spectral Classification	Ref.
(1)	(2)	(3)	(4)	(5)	(6)	(7)	(8)	(9)	(10)	(11)	(12)
	1068	SA(rs)b	3	14.4	7.08	29	9.61	1135	−20.0	S1.8	1
	3227	SAB(s)a pec	1.2	20.6	5.37	56	11.10	1146	−19.8	S1.5	2
1	2655	SAB(s)0/a	0.1	24.4	4.90	34	10.96	1403	−20.9	S2	3
	4459	SA(r)0	-1.4	16.8	3.55	41	11.32	1202		T2	3
2	3627	SAB(s)b	3.0	6.6	9.12	65	9.65	727	−17.2	S2/T2	3
	5806	SAB(s)b	3.3	28.5	3.09	58	12.40	1359		H	4
3	4051	SAB(rs)bc	4.2	17.0	5.25	43	10.83	720	−18.2	S1.2	3
	5248	SAB(rs)bc	4.2	22.7	6.17	40	10.97	1152		H	5
4	4151	SAB(rs)ab	2	20.3	6.31	21	11.50	992	−19.7	S1.5	6
	2985	SA(rs)ab	2	22.4	4.57	38	11.18	1218		T2	3
5	4579	SAB(rs)b	2.8	16.8	5.89	38	10.48	1521	−19.4	S1.9/L1.9	3
	3351	SB(r)b	2.9	8.1	7.41	56	10.53	778		H	7
6	5194	SA(rs)bc pec	4.2	7.7	11.22	20	8.96	463	−16.0	S2	8
	5055	SA(rs)bc	4	7.2	12.59	56	9.31	504		T2	3
7	6951	SAB(rs)bc	3.9	24.1	3.89	34	11.64	1424	−17.9	S2	9
	5248	SAB(rs)bc	4.2	22.7	6.17	40	10.97	1152		H	5

Table 1. Properties of our sample. (1) Pairs identifier, (2) Galaxy name, (3) Hubble Type (NED), (4) Numerical morphological type (LEDA), (5) Distance in Mpc (Ho et al. 1997), (6) D_{25} in arcmin (Ho et al. 1997), (7) disc inclination in degrees, (8) Total apparent magnitude B_T in mag (Ho et al. 1997), (9) Systemic velocity in $km\,s^{-1}$ (NED), (10) V-band absolute magnitude of the Seyfert nuclei M_V in mag (Ho et al. 1997), (11) Spectral classification (Ho et al. 1997): H=HII nucleus, S=Seyfert nucleus, L=LINER, T=transition object, 'T2' implies that no broad Hα emission lines was detected (Ho et al. 1997). (12) References for the disc inclination values. 1: García-Gómez et al. (2002), 2: Mundell et al. (1995), 3: Ho et al. (1997), 4: Kassin et al. (2006), 5: Jogee et al. (2002), 6: Pedlar et al. (1992), 7: Erwin (2005), 8: Tully (1974), 9: Rozas et al. (2002)

ionised gas emission lines (Hβ, [O III] and [N I]). More details on the SAURON spectrograph can be found in Bacon et al. (2001). Fig. 1 presents the SAURON field-of-view overlaid on R-band Digital Sky Survey (DSS) images of our galaxies.

The data of the 15 galaxies were reduced using the dedicated XSAURON software and an automatic pipeline available within the SAURON consortium (Bacon et al. 2001; de Zeeuw et al. 2002). The main steps include: bias and dark subtraction, extraction of the spectra using a mask, wavelength calibration, low-frequency flatfielding, cosmic rays removal, homogenisation of the spectral resolution in the field, sky subtraction (using 146 sky spectra 1.9 arcmin away from the main field). Then the flux calibration was applied as explained in detail in Kuntschner et al. (2006). The flux calibrated individual exposures are then accurately centred with respect to each others and merged. The final merged datacube is sampled onto a squared grid with $0\farcs8 \times 0\farcs8$ pixels.

Finally, the point spread function (PSF) of each merged exposure was determined by comparing the reconstructed SAURON intensity distribution with HST/WFPC2 images. The SAURON PSF is modeled by a single 2D Gaussian, whose parameters is determined by minimizing the differences between the HST/WFPC2 images, convolved by this Gaussian and the SAURON reconstructed images. The derived seeing values (Full Width at Half Maximum) are listed in Table 2.

2.3 Derivation of Stellar Kinematics

In order to ensure the reliability of the stellar kinematic measurements, the merged datacubes were spatially binned using the Voronoi 2D binning algorithm of Cappellari & Copin (2003), creating bins with a minimum signal-to-noise ratio (S/N) = 60 per bin. The stellar contribution to the SAURON spectra is potentially contaminated by emission lines: H$\beta\,\lambda$4861, [O III]$\lambda\lambda$4959,5007 and [N I]$\lambda\lambda$5198,5200, therefore we first identified and masked out the spectral regions that are significantly contaminated by emission. The stellar kinematics are measured on each spectrum in our binned datacubes using the penalized pixel fitting (pPXF) method developed by Cappellari & Emsellem (2004). The line-of-sight velocity distribution (LOSVD hereafter) is parameterised by Gauss-Hermite series and the algorithm determines the mean velocity V, the velocity dispersion σ and the higher Gauss-Hermite moments h_3 and h_4 which minimize the differences between the observed spectrum and a stellar template spectrum convolved with the corresponding LOSVD. A low-order polynomial is included to account for small differences between the galaxy and the template spectra. A first estimate of the kinematic parameters is done using a single star spectrum as template. Then using this initial estimate, an optimal stellar template is derived for each individual spectrum, via the use of a large library of stellar templates (Vazdekis 1999). We finally iterate by measuring best-fitting values at each position for the velocity V, the velocity dispersion σ, h_3 and h_4 using this time the optimal templates obtained from the previous step. The stellar

Pairs	Name NGC	dates	T_{exp} (s)	FWHM$_{PSF}$ (arcsec)
(1)	(2)	(3)	(4)	(5)
	1068	2002 January	300 + 3x1800	1.9±0.1
	3227	2004 March	3x1800	1.4±0.2
1	2655	2004 March	6x1800	1.4±0.1
	4459	2001 March	4x1800	1.6±0.1
2	3627	2004 March	4x1800	1.6±0.1
	5806	2004 March	2x1800	2.1±0.1
3	4051	2004 March	6x1800	1.4±0.2
	5248	2004 March	5x1800	1.9±0.1
4	4151	2004 March	3x1800	2.0±0.3
	2985	2004 March	3x1800	1.2±0.1
5	4579	2004 March	4x1800	1.9±0.1
	3351	2004 March	4x1800	0.9±0.1
6	5194	2004 March	4x1800	1.2±0.1
	5055	2004 March	6x1800	2.4±0.1
7	6951	2003 August	3x1800	1.4±0.1
	5248	2004 March	5x1800	1.9±0.1

Table 2. Details of the exposures of our sample. (1) Pairs identifier, (2) NGC number, (3) date of observation (4) Exposure time in sec, (5) Seeing, Full Width at Half Maximum in arcseconds.

kinematic parameters were determined using this method automatically implemented in the `SAURON` data reduction pipeline for our whole sample except for the Seyfert 1 galaxies: NGC 3227, NGC 4051 and NGC 4151. For these galaxies, the automatic pipeline alone is inadequate due to the presence of a broad Hβ emission line in the inner few arcseconds (see Fig. 2.c). The spectral regions that are masked have to be carefully defined, and then we fit the stellar kinematics of these 3 galaxies interactively.

The AGN continuum is not separated from the stellar component using this technique. The stellar kinematic derivation of the Seyfert 2s is a priori not affected by the AGN continuum since the central engine is hidden from direct view. The AGN continuum would however affect the derivation of the velocity dispersion of the Seyfert 1s in the central regions where it is dominant. These regions have been excluded from the stellar kinematic analysis and subsequent discussion.

2.4 Derivation of Gaseous Distribution and Kinematics

The stellar continuum resulting from the stellar kinematic fit was subtracted from the original data, providing pure emission line datacubes. The wavelength range of our observations includes the Hβ λ4861, [O III]$\lambda\lambda$4959,5007 and [N I]$\lambda\lambda$5198,5200 emission lines. The parameters of these emission lines (intensity, mean velocity and FWHM) were derived from Gaussian fitting using the `fit/spec` software developed by Rousset (1992).

The fit was performed on two systems of emission lines : the first consisting of the Hβ and [N I] lines, and the second, of the [O III] lines. The Hβ and [O III] lines were fitted independently in order to detect differences in the kinematics of the two lines. Since the [N I] lines are significantly weaker than the Hβ and [O III] lines, their kinematics can not be constrained independently, therefore this doublet is fitted together with the Hβ line system. Within each system, the lines were assumed to share the same velocity and FWHM. Constraints were applied on the parameters: the line ratio [O III]λ4959/[O III]λ5007 was assumed throughout to be equal to 2.88, and $0.5 <$ [N I]λ5198/[N I]λ5200 < 1.5. Moreover the velocity V and the velocity dispersion FWHM of the lines were bounded: V around the systemic velocity of the galaxy, and the FWHM by the spectral resolution of `SAURON` FWHM$_{\texttt{SAURON}} = 4.2$ Å. Usually the line profiles were simple enough to be fitted automatically. A first fit was done using one single Gaussian profile and this automated fit has been visually controlled for each galaxy. An example of the emission lines fitting results is given in Fig. 2.a. A small number of galaxies show complex emission lines profiles and required a manual fit with additional emission line components. Additional components for [O III] lines, Hβ line or both were required in the case of five active galaxies: NGC 3227 (Fig. 2.b), NGC 4051, NGC 4151 and NGC 5194. These additional components are certainly associated with the Narrow Line Regions (NLR) of these galaxies. An unresolved central Hβ broad component has also been added in the case of the Seyfert 1 galaxies (NGC 3227, NGC 4051 and NGC 4151) which corresponds to the Broad Line Regions (BLRs). The FWHM of this component is 2600 km s^{-1}, 1500 km s^{-1} and 3100 km s^{-1} for NGC 3227, NGC 4051 and NGC 4151, respectively, and the spatial extent of the radial profile of the BLRs (Fig. 3) is consistent with the PSF derived above, within the derived uncertainties (Table 2). Finally, in the case of NGC 4051, FeII blends are detected as shown in Fig. 2.d, and these emission lines were therefore added in the fit for this galaxy.

3 RESULTS

In this Section, we present the distribution and kinematic maps of the stellar and ionised gas components for our sample of galaxies. Figures 4a to 4h present our `SAURON` maps: stellar continuum, [O III] and Hβ intensity distributions and emission line ratio [O III]/Hβ, as well as stellar and gaseous kinematics (velocity and velocity dispersion). In the case of the Seyfert 1 galaxies, the line ratio [O III]/Hβ is computed using the narrow Hβ component. The galaxies are displayed by pair: the Seyfert on the top, its control galaxy below, except for NGC 1068 and NGC 3227 which are shown together (Fig. 4a). All the maps are oriented so that the outer photometric major-axis of the galaxy is on the horizontal axis. To display the gas maps, we show only the reliable emission, i.e. when the ratio of the fitted amplitude to the surrounding noise is larger than 3. The [N I] doublet is detected in most of our galaxies, but it is very weak, so it is not discussed further. The gaseous kinematic maps (velocity and dispersion) correspond to the [O III] emission lines kinematics, except for the inactive galaxy NGC 4459 (Fig. 4b) for which the Hβ line was used since it is slightly more extended and has a better signal-to-noise ratio (Fig. 4c). The Hβ emission line velocity and velocity dispersion maps are shown in Appendix B ([O III] corresponding maps for NGC 4459).

Finally, NGC 4459 and NGC 6951 were observed as part

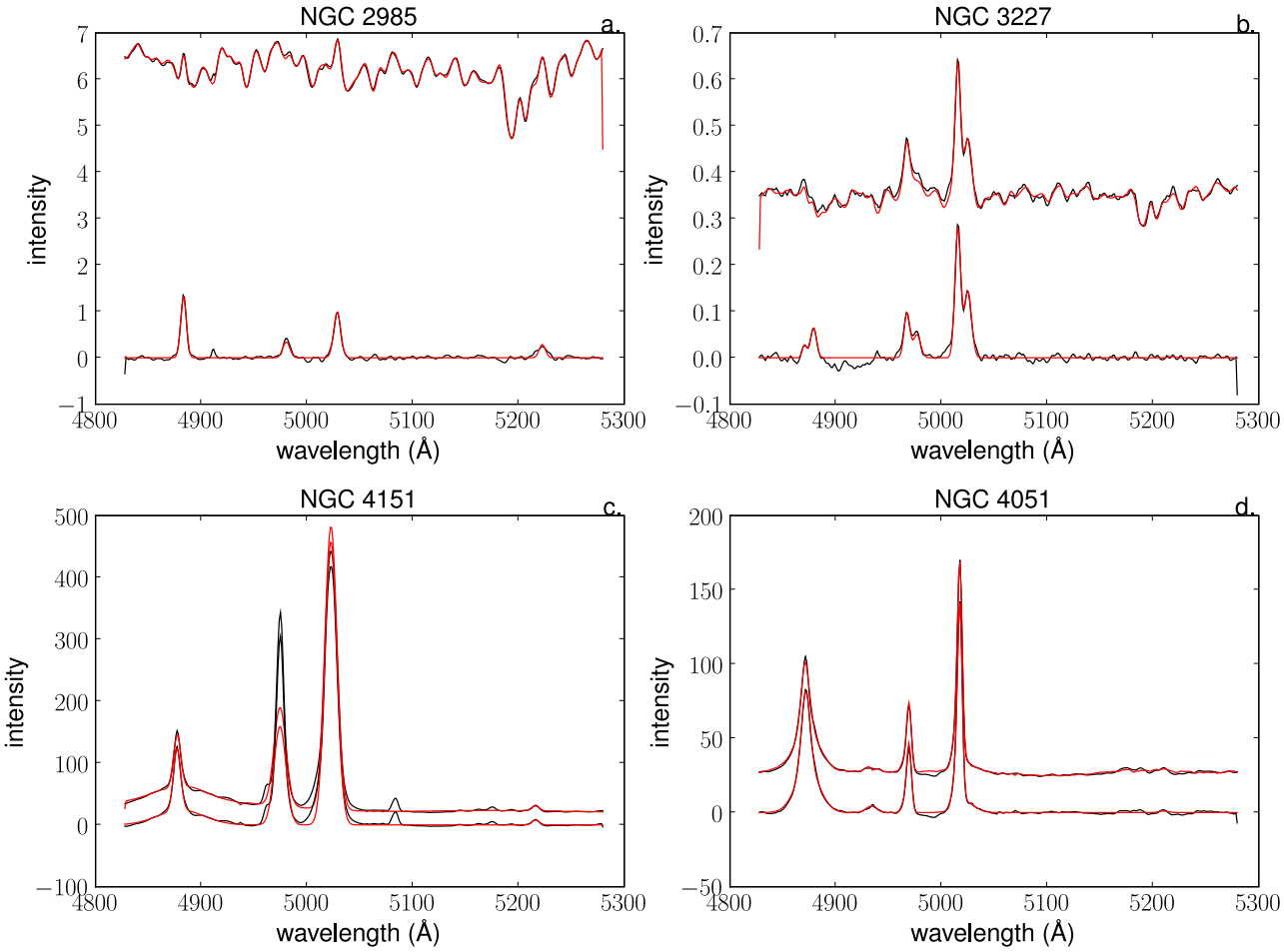


Figure 2. Examples of spectra and their corresponding fits for 4 galaxies. (a): NGC 2985 (inactive), (b): NGC 3227 (Seyfert 1.5), (c): NGC 4151 (Seyfert 1.5), (d): NGC 4051 (Seyfert 1.2). In each panel, the black line on the top shows the galaxy spectrum and the red line, its corresponding fit which is composed of the best-fitting stellar template added to the emission line fit. Below this spectrum, the pure emission line spectrum is shown in black. The corresponding emission lines fit is overplotted in red. The spectra were taken in the central pixel of the FOV, except for NGC 3227, for which the spectrum was taken at 4″ North-East from the center.

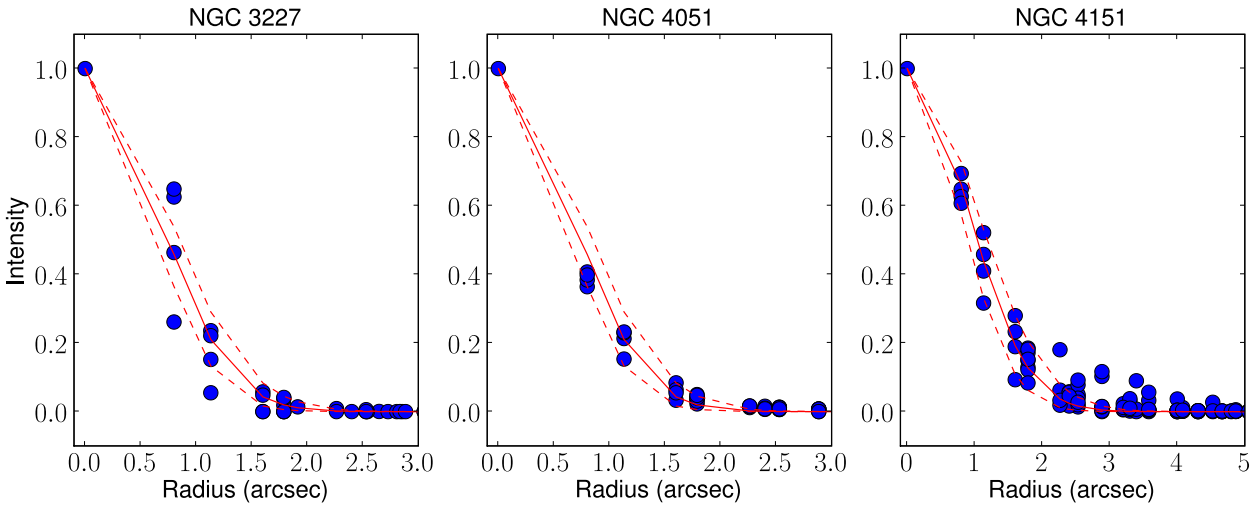


Figure 3. Radial normalised profiles of the BLR for NGC 3227, NGC 4051 and NGC 4151 (filled blue circles). The red solid line corresponds to the best-fit seeing value for each of the three galaxies (see Table 2), the two red dashed curves correspond to the associated upper and lower limits at 2σ.

of other programmes (de Zeeuw et al. 2002) with multiple fields to provide a mosaic (Fig. 1). For consistency with the other galaxies in our sample, we extracted images corresponding to one single SAURON field of view (FOV) from the mosaiced exposures for these two galaxies.

In the following we present the general properties of our sample. Detailed descriptions of the maps for each galaxy can be found in Appendix A.

3.1 Stellar and Ionised Gas Distribution

For each galaxy, the stellar continuum maps (Figs. 4a-4h, first panel for each galaxy) were derived by integrating over the full wavelength window the spectra corresponding to the optimal stellar template obtained as explained in Sect. 2.3. We constructed the ionised gas intensity maps and the [O III]/Hβ lines ratio maps directly from the fit of the emission lines spectra.

3.1.1 Stellar Continuum Distribution

Half of the galaxies in our sample present symmetric stellar continuum maps with regular isophotes. NGC 2985, NGC 4151 (Fig. 4e) and NGC 4459 (Fig. 4b) show rather round central features while the isophotes are more flattened for NGC 3227 (Fig. 4a), NGC 4051 (Fig. 4e), NGC 5806 (Fig. 4c) and NGC 6951 (Fig. 4h). The latter four galaxies host a large scale stellar bar, their stellar continuum reflecting the elongation of the bar in the central regions.

Five Seyfert 2 galaxies and one inactive galaxy present more complex stellar distribution maps. Isophotal twists or irregular isophotes are observed in five Seyfert 2 galaxies: NGC 1068 (Fig. 4a), NGC 2655 (Fig. 4b), NGC 3627 (Fig. 4c), NGC 4579 (Fig. 4f) and NGC 5194 (Fig. 4g). The inactive galaxy NGC 5055 presents an asymmetric structure (Fig. 4g). The surface brightness is higher on the North-West side of the FOV, the emission line flux being absorbed by the dust on the South-East (see Fig. 1). The predominance of irregular isophotes and twists in the circumnuclear regions of Seyfert 2 galaxies compared to Seyfert 1 or inactive galaxies has been described quantitatively by Hunt & Malkan (2004).

Finally, two inactive galaxies, NGC 3351 and NGC 5248 exhibit a circumnuclear ring at a radius of $\sim 5''$ which corresponds to 550 pc for NGC 3351 and 200 pc for NGC 5248, respectively. These structures have been described by Devereux et al. (1992) and Laine et al. (2001).

3.1.2 Ionised Gas Distribution

Ionised gas is detected in all the galaxies of our sample, over the full SAURON FOV except for NGC 4459 (Fig. 4b), where emission lines are very weak outside the inner $10''$. In this Section we describe the maps of the gas properties mainly focusing on regions which are not dominated by non-gravitational motions driven by the active nucleus.

A variety of structures can be seen in the [O III] and Hβ intensity maps:

- Spiral-like structures are seen in two Seyfert galaxies: NGC 1068 (Fig. 4a, Hβ intensity map) and NGC 4579 (Fig. 4f). Such structures correspond well with the nuclear molecular spirals observed by Schinnerer et al. (2000) and García-Burillo et al. (2005) in NGC 1068 and NGC 4579, respectively.
- Circumnuclear rings are found in three inactive galaxies (NGC 3351 Fig. 4f, NGC 5248 Fig. 4d and NGC 5806 Fig. 4c) and the Seyfert 2 NGC 6951 (Fig. 4h), which correspond with known ring-like star forming structures in the central regions of these four galaxies (Devereux et al. 1992; Laine et al. 2001; Carollo et al. 2002, respectively).
- In five other galaxies, asymmetric structures are observed. The emission line distribution of NGC 4151 is elongated from the centre to the South-West side of the FOV (Fig. 4e) in agreement with the high-excitation emission line feature described by Perez et al. (1989), corresponding to the Extended Narrow Line Regions (ENLR) of this galaxy. The Seyfert 2 galaxy NGC 2655 (Fig. 4b) presents a hot-spot $15''$ away from the centre to the East and a lane $10''$ West of the centre elongated along the South/North direction consistent with the polar ring observed by Keel & Hummel (1988). Asymmetric and irregular structures observed in the ionised gas intensity maps of NGC 3627 (Fig. 4c) or NGC 5055 (4g) are certainly due to the presence of dust in the circumnuclear regions. In the case of NGC 5194 both the stellar continuum and the Hβ emission line intensity present irregularities consistent with the dusty nuclear spiral (Peeples & Martini 2006), while [O III] emission lines traces an outflow structure associated with the AGN.
- Finally three galaxies (two inactive NGC 2985, Fig. 4e, NGC 4459, Fig. 4b and the Seyfert 1 NGC 4051, Fig. 4d) show regular round gaseous distributions.

3.1.3 Ionised Gas Line Ratios

As expected, the Seyfert galaxies present higher [O III]/Hβ ratios than their associated inactive galaxies in the central kpc regions. The maximum measured ratio for the inactive galaxies is of the order of 2, while for Seyfert galaxies it can reach values up to 10 or 20. For the Seyfert galaxies, the emission line ratio reaches its highest value in the central few arcseconds associated with the active nucleus. Some regions away from the central engine are also characterised by high [O III]/Hβ values ($\gg 1$) corresponding to high excitation regions, such as in the ionisation cone of NGC 1068 (Fig. 4a), the bubble of NGC 5194 (Fig. 4g) or the elongated gaseous feature of NGC 4151 (Fig. 4e). Finally the ring-like structures seen in the gaseous maps of NGC 3351, NGC 5248 and NGC 5806 show low emission lines ratios ([O III]/H$\beta \lesssim 0.1$) consistent with star formation.

3.2 Stellar and Ionised Gas Kinematics

Outside the regions dominated by non-gravitational motions associated with AGN-driven outflows, all of our galaxies show stellar and gas velocity fields with a global regular rotation pattern (second panel of each row in Figs. 4a to 4h). More complex dynamical structures are observed in some cases, especially in the ionised gas velocity fields.

3.2.1 Stellar Kinematics

Most of the galaxies in our sample present a regular stellar velocity field, the orientation of their kinematic major-axis being constant over the FOV and their minor-axis perpendicular to it (e.g. NGC 2985 Fig. 4e, NGC 4459 Fig. 4b, NGC 5055 Fig. 4g). A few active galaxies show some departures from axisymmetry e.g. the S-shaped zero-velocity line in NGC 1068 (Fig. 4a) and twisted kinematic major-axis in NGC 3627 (Fig. 4c). In all of our sample galaxies, the stellar kinematic major-axis is rather well aligned with the outer disc photometric major-axis (see Sect. 4.1.1). The observed stellar kinematics within the SAURON field of view are also clearly dominated, in all cases, by rotational motion, as evaluated via a global measurement of V/σ (Dumas et al., in preparation), confirming the disc-like nature of the galaxies in our sample.

For some of our galaxies, the stellar velocity dispersion decreases inwards. These so-called σ-drops (Emsellem et al. 2001; Márquez et al. 2003) are observed in at least five Seyfert galaxies NGC 1068, NGC 2655, NGC 3227, NGC 4051, NGC 4151 and NGC 6951 and one inactive galaxy NGC 5248. These central σ-drops have been found to be common in S0 to Sb spiral galaxies (Emsellem et al. 2004; Falcón-Barroso et al. 2006; Márquez et al. 2003) and recently Ganda et al. (2006) showed that such structures are present in galaxies as late as Sd. Central velocity dispersion drops are thought to be associated with dynamically cold structure, like discs and star formation regions (Wozniak et al. 2003).

3.2.2 Ionised Gas Kinematics

The ionised gas velocity maps are dominated by rotation and for all of the galaxies the gas rotates faster than the stars (Figs. 4a to 4h second panels of the second rows). Since stars follow collisionless orbits, their mean velocities are indeed expected to be lower than the local circular velocity (see Binney & Tremaine 1987). The gas velocity fields are more distorted and present richer structures than the stellar ones. Evidence for significant deviations from axial symmetry exist in almost all the galaxies: radial change of orientation of the major-axis (NGC 3227, Fig. 4a), wiggles along the kinematic minor-axis (NGC 2655, Fig. 4b , NGC 4579, Fig. 4f), S-shaped feature (NGC 1068, Fig. 4a), or more complicated structures (e.g. NGC 3627, Fig. 4c or NGC 5194, Fig. 4g). For all of our galaxies, the Hβ and [O III] velocity fields present very similar structure, though [O III] velocity fields have generally better signal-to-noise ratio than the Hβ ones, except for NGC 4459 (Figs. 4a and B1a). We also observe highly misaligned kinematic major-axes of the ionised gas with respect to the stellar ones in some of our galaxies such as NGC 2655 (Fig. 4b) and NGC 4579 (Fig. 4f). These misalignments will be analysed in the following Section.

The gaseous velocity dispersion maps present no particular structure for all of the inactive galaxies and two Seyferts (NGC 3627, Fig. 4c and NGC 4051, Fig. 4d). For eight Seyfert galaxies (NGC 1068, NGC 2655, NGC 3227, NGC 3627, NGC 4151, NGC 4579, NGC 5194 and NGC 6951) and three inactive galaxies (NGC 2985, NGC 4459 and NGC 5055) σ values increase inwards. In the inner 5″, the dispersion can reach values 200 km s^{-1} higher than in the outer part of the FOV as in NGC 1068 (Fig. 4a). NGC 2655 (Fig. 4b) and NGC 4579 (Fig. 4f) also present high dispersion values ($\sim$ 230 km s^{-1}) associated with the gas distribution structures. For NGC 4151, gaseous dispersion velocity maps exhibit high values in the inner arcseconds (about 280 km s^{-1}) corresponding to the central engine. Outside the very inner part and inside the ENLR, the velocity dispersion shows lower values (between 50 and 130 km s^{-1}). Then, σ increases in the outside parts of the map for this galaxy, corresponding to the location of a dusty ring (Vila-Vilaro et al. 1995).

4 COMPARISON OF STELLAR AND GASEOUS KINEMATICS

In the previous Section we described the SAURON maps of the stellar and ionised gas components for the Seyfert and inactive galaxies. For all of our galaxies, the stellar velocity fields are dominated by rotation, showing regular isovelocity contours and their photometric and kinematic major-axes seem globally aligned. In comparison with the stellar maps, however, the gaseous distributions are more complex and the kinematics more perturbed with this effect appearing more pronounced for the Seyferts compared to their control galaxies. The identification of this qualitative difference between gaseous and stellar distributions and kinematics in the inner kpc of active and inactive galaxies has important implications for the triggering and nuclear fueling. In this Section, we therefore provide a more quantitative analysis of the stellar and gaseous velocity fields and the photometric major-axis of the galaxies. We first compare the major-axis orientation of the stellar velocity field to that of the outer galactic disc. Then we quantify the differences between stars and gas in Seyfert and inactive galaxies as seen in our SAURON maps. We compare the global orientation of the stellar and ionised gas kinematic maps to probe any significant differences between the two components. Then we analyse the kinematic maps in more detail, by computing the kinematic parameters (systemic velocity, dynamical centre, PA, rotational velocity) as a function of radius, using a simple representation of a two-dimensional thin disc in rotation.

4.1 Global Kinematic Major-Axis Orientation

The stellar and gaseous velocity fields can be first simply parameterised by their major-axes. Misalignments between the kinematic major-axis of the stellar and ionised gas components may reveal the presence of non-axisymmetric structures or decoupled components such as central discs. Here, we compare such misalignments in our sample of Seyfert and control galaxies, to characterise global kinematic differences in their central kpc.

The kinematic axis orientations were determined for both the stellar and ionised gas velocity fields. The global position angles (PAs) of the kinematic major-axis were obtained by minimizing the differences between our SAURON velocity fields (stars and [O III]) and a bi-antisymmetric representation of these fields. This method is detailed by Krajnović et al. (2006) in their Appendix C and we used a specific implementation written by Michele Cappellari. The val-

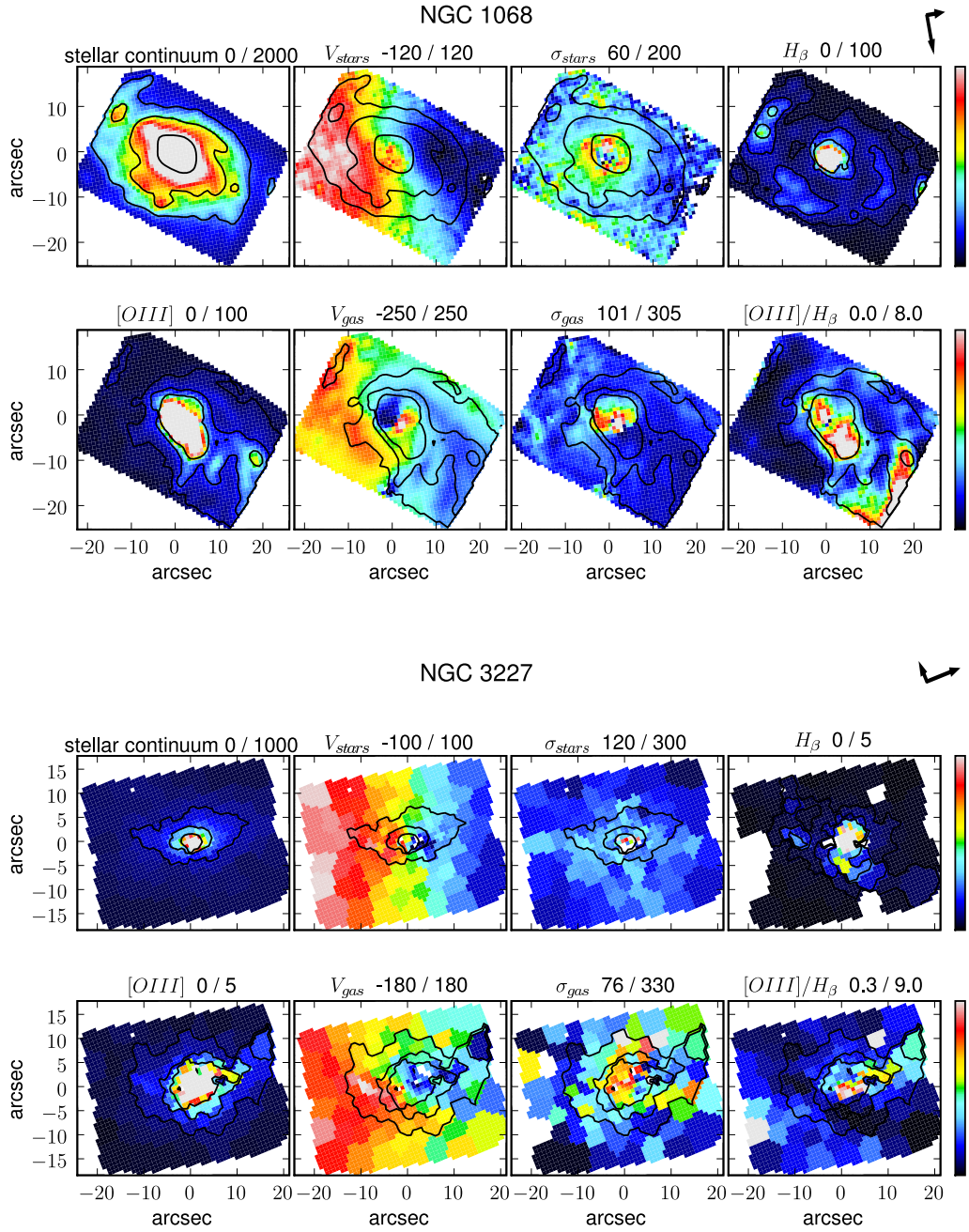


Figure 4a. SAURON maps for the Seyfert galaxies NGC 1068 (top panels) and NGC 3227 (bottom panels). For each galaxy the first row shows (from left to right) the reconstructed continuum map, the stellar velocity field, the stellar velocity dispersion map and Hβ intensity distribution. The second row consists of the [O III] intensity velocity and velocity dispersion maps and the line ratio [O III]/Hβ map. All the intensity maps are in units of 10^{-16} erg s^{-1} cm^{-2}. The stellar and emission lines intensity maps are overlaid on the stellar and ionised gas kinematics. Velocities and velocity dispersions are in km s^{-1}. The color scale is shown on the right hand side and the cut levels are indicated in the top right corner of each map. All the maps are orientated so that the photometric major-axis of the galaxy is on the x-axis. The long and short arrows on the right of each galaxy name show the North and the East directions, respectively.

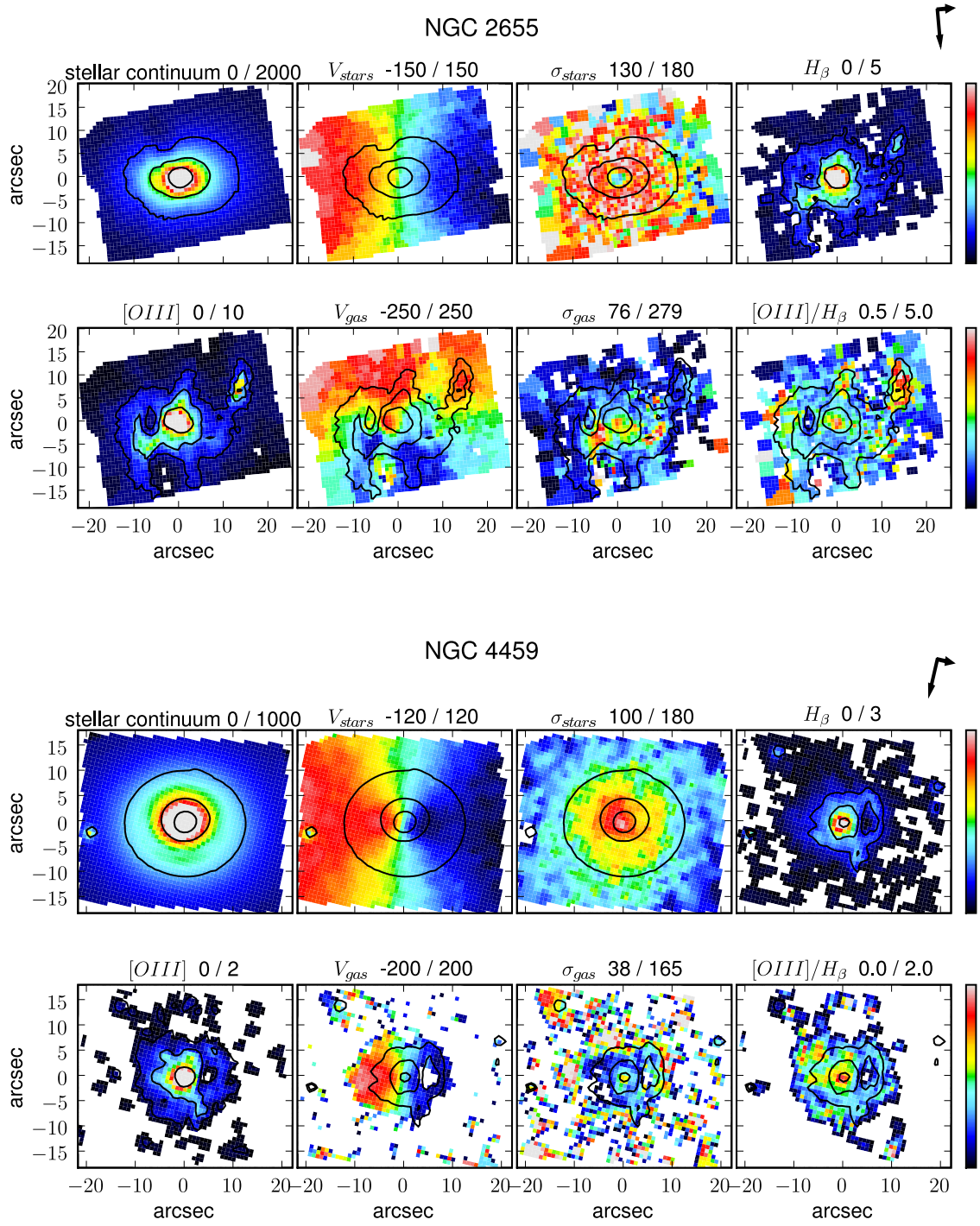


Figure 4b. SAURON maps for NGC 2655 (top panels) and its control NGC 4459 (bottom panels). See caption of Fig. 4a for details.

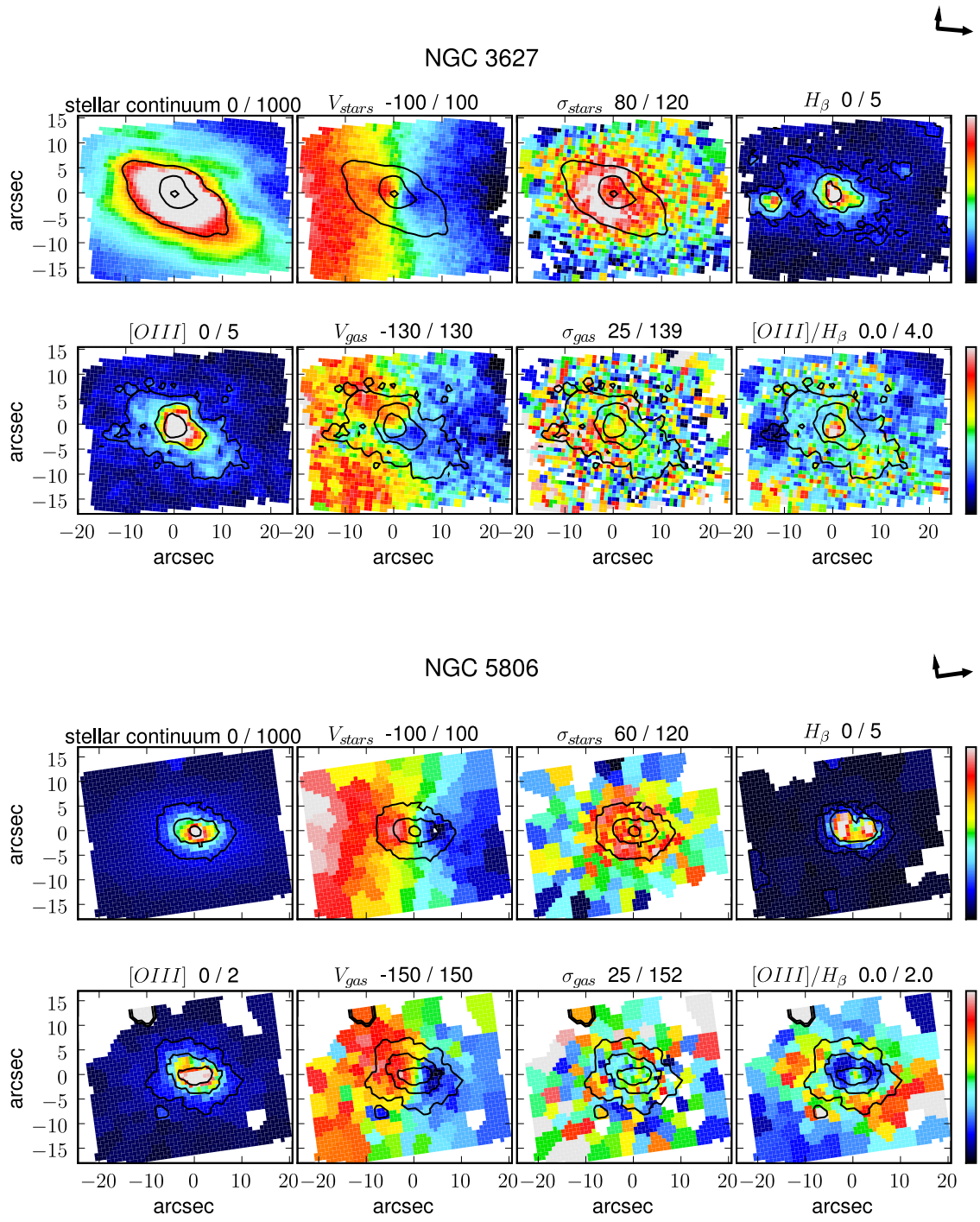


Figure 4c. SAURON maps for NGC 3627 (top panels) and its control NGC 5806 (bottom panels). See caption of Fig. 4a for details.

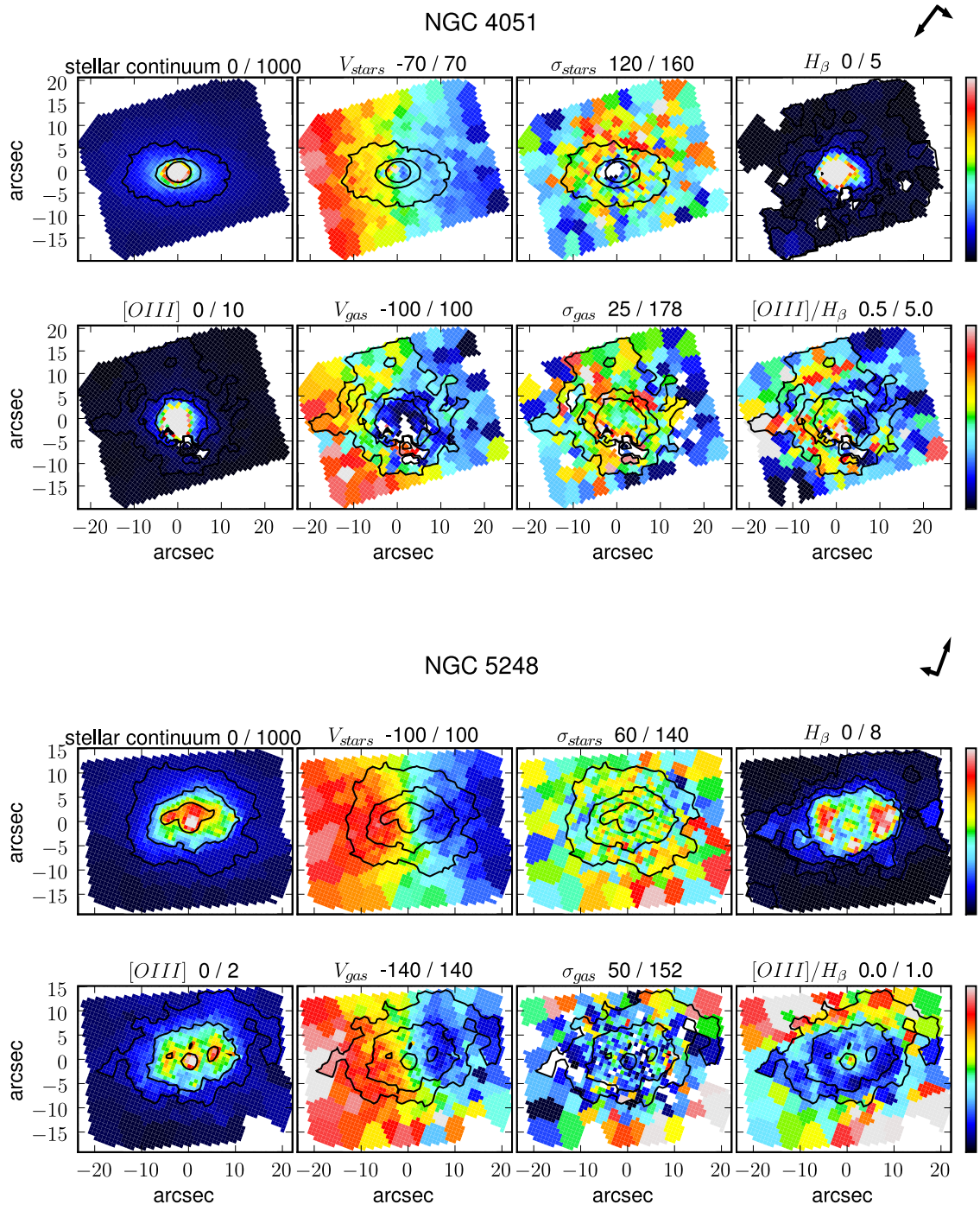


Figure 4d. SAURON maps for NGC 4051 (top panels) and its control NGC 5248 (bottom panels). See caption of Fig. 4a for details.

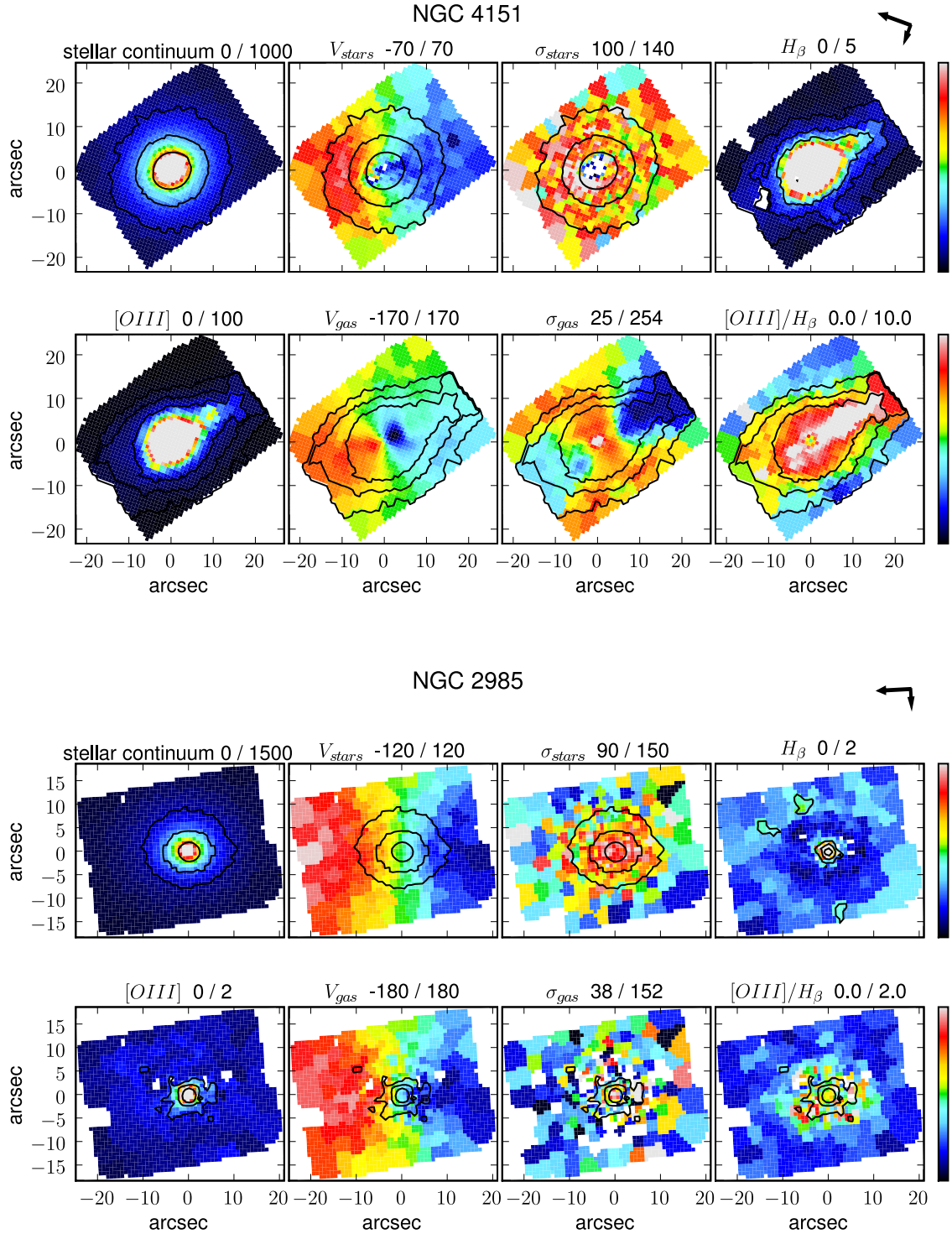


Figure 4e. SAURON maps for NGC 4151 (top panels) and its control NGC 2985 (bottom panels). See caption of Fig. 4a for details.

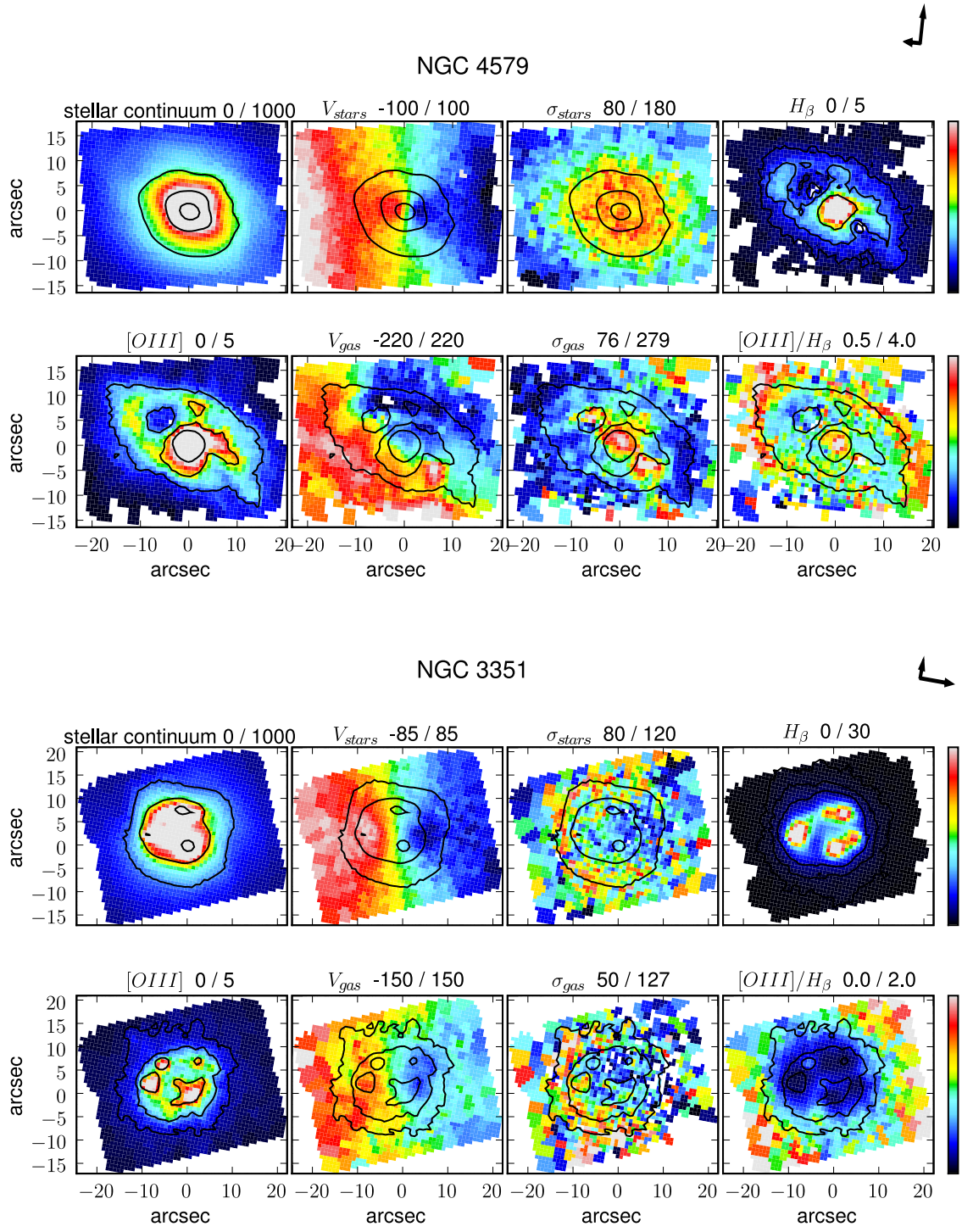


Figure 4f. SAURON maps for NGC 4579 (top panels) and its control NGC 3351 (bottom panels). See caption of Fig. 4a for details.

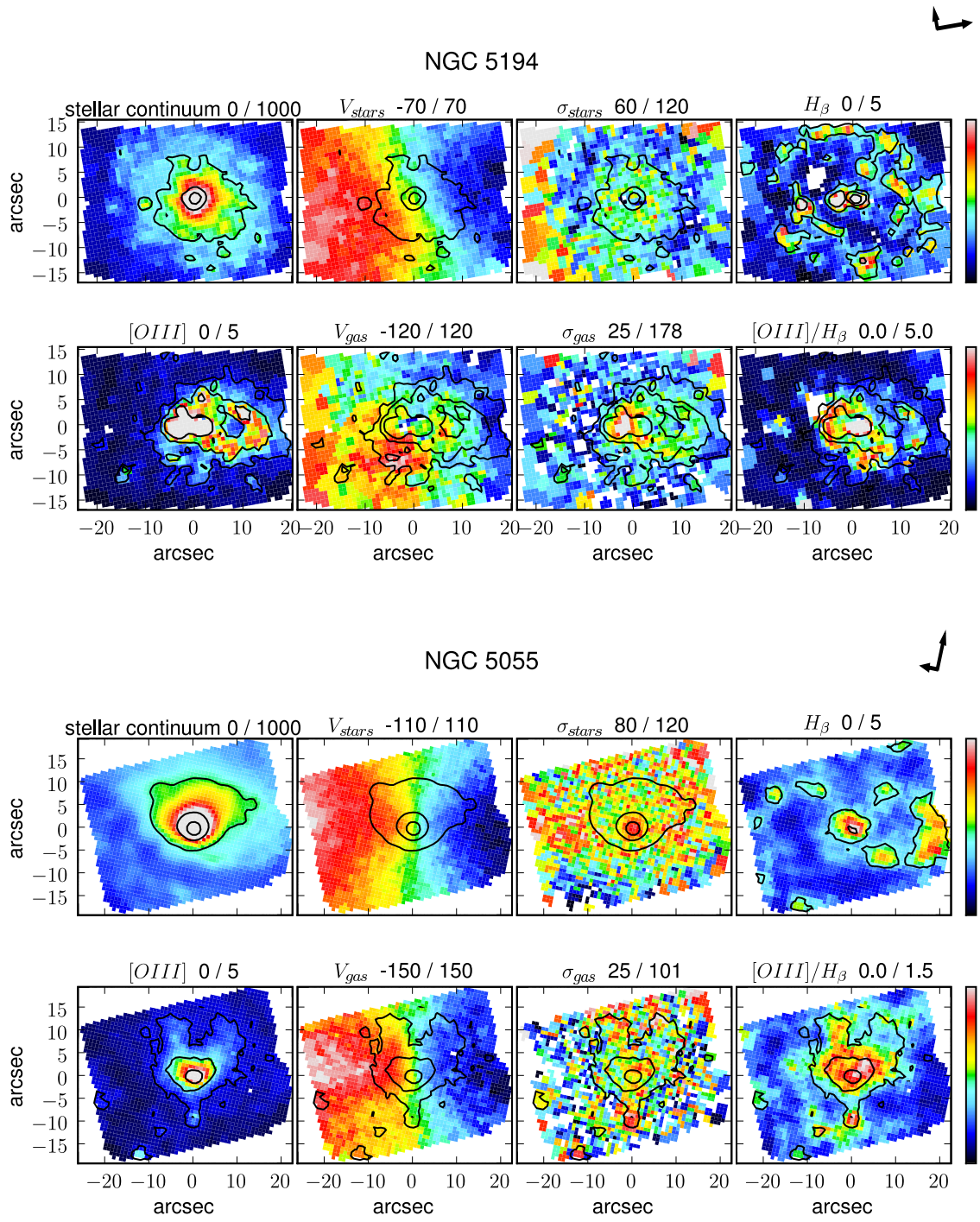


Figure 4g. SAURON maps for NGC 5194 (top panels) and its control NGC 5055 (bottom panels). See caption of Fig. 4a for details.

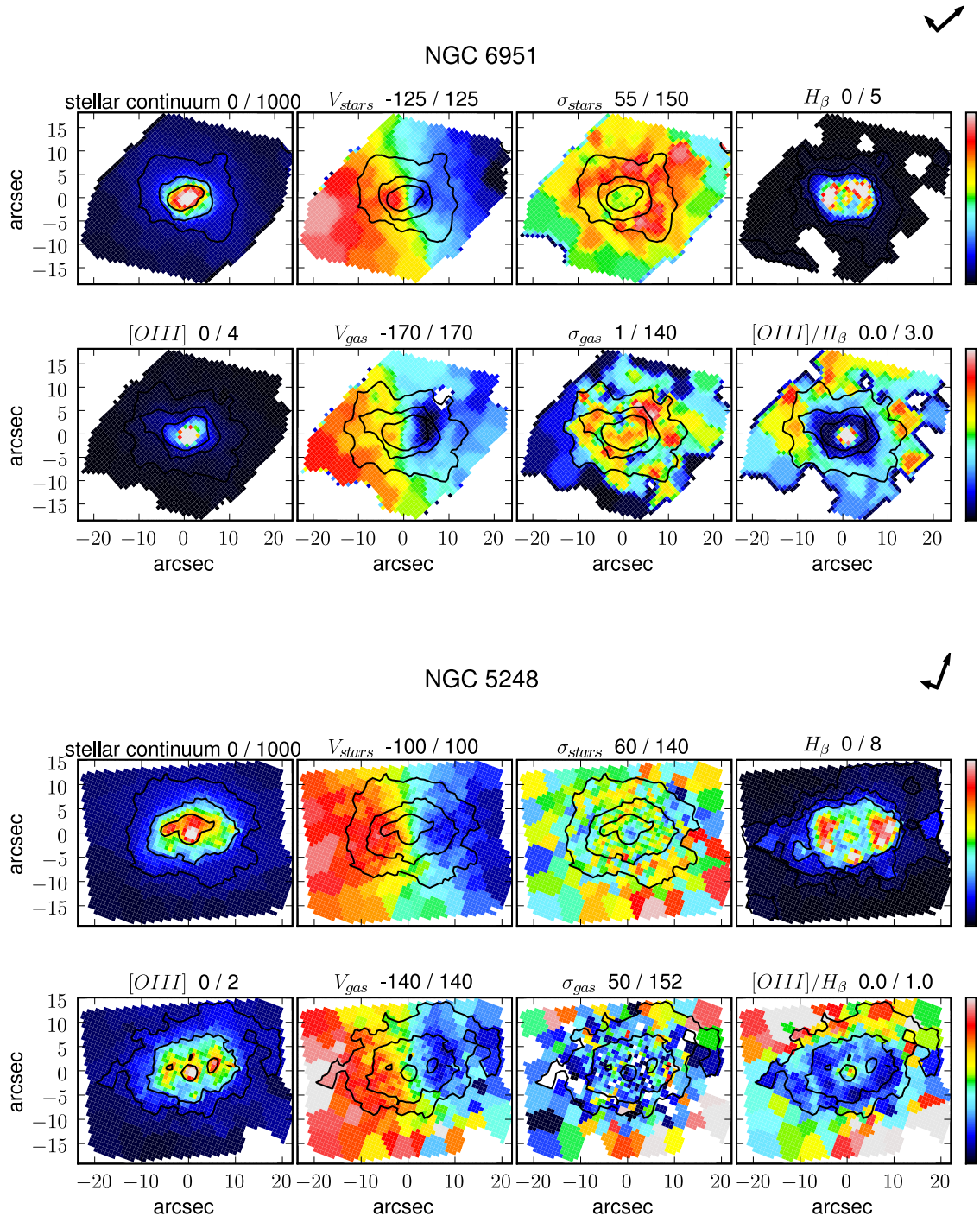


Figure 4h. SAURON maps for NGC 6951 (top panels) and its control NGC 5248 (bottom panels). See caption of Fig. 4a for details.

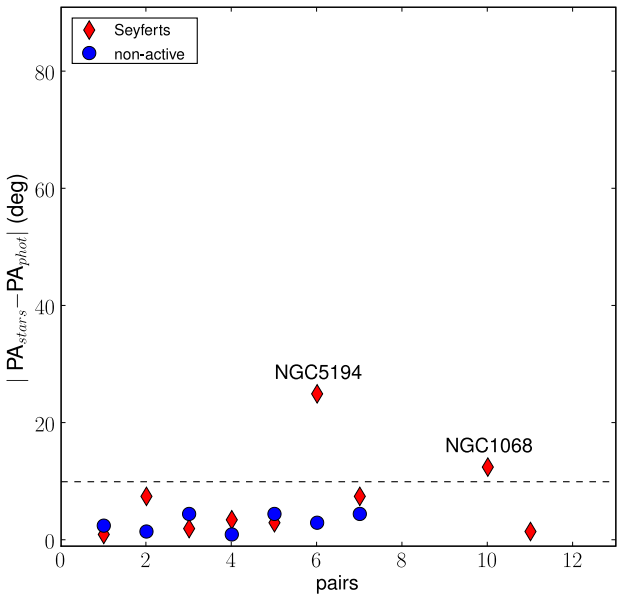


Figure 5. Distribution of the differences between the photometric and the global stellar kinematics PAs $PA_{stars} - PA_{phot}$ for each pair of galaxies, Seyferts (red diamonds) and inactive galaxy (blue circles). The dashed black horizontal line corresponds to a difference of 10°.

ues for the measured kinematics PAs and misalignments are listed in Table 3.

4.1.1 Stellar Kinematic and the Orientations of the Line of Nodes

In the case of an axisymmetric mass distribution, the direction of the stellar kinematic major-axis should coincide with the line-of-nodes (LON) of the galaxy, while in the case of a triaxial potential the kinematic and photometric major-axes can depart from each other due to projection effects. We first therefore check if the stellar kinematic major-axis in the central regions and the outer photometric major-axis are aligned. The photometric major-axis position angle is computed from ellipse fitting on the R-band DSS images for each of our galaxies. These derived values are then compared with published ones. For most of our galaxies, the PAs values found in the literature are in good agreement with those derived from the ellipse fit, within the error bars, in which case we took our measured values as the photometric PAs. However, a few galaxies present significant discrepancies between our fitted values and the published ones. This is the case for NGC 1068 and NGC 4151 which present a weak oval bar and a faint, almost circular outer disc, respectively. The measurement of the photometric PA of NGC 5194 is uncertain given that this galaxy is nearly face-on (i=20°). We therefore used reliable values derived from HI kinematics for NGC 4151 (Pedlar et al. 1992) and optical kinematics for NGC 5194 (Tully 1974), as the photometric PAs. Table 3 lists the resultant photometric PA values for the sample galaxies. The differences between the global stellar kinematic and the photometric PAs are plotted in Fig. 5.

Our first qualitative impression is confirmed: the stellar kinematic PAs are parallel to the photometric ones within 10° for all of our galaxies except for NGC 5194 and NGC 1068 which present a difference of about 20° and 15°, respectively. In the case of NGC 1068, the stellar kinematic major-axis PA corresponds to the average PA of the kinematic axis as fitted on the large-scale HI data by Bland-Hawthorn et al. (1997), while the outer photometric major-axis lies at a PA of about 80°(Emsellem et al. 2006). Besides the two specific cases of NGC 5194 and NGC 1068, for all of our galaxies the major-axis orientation of the central part of the stellar velocity field is therefore a reliable measurement for the line-of-nodes of the galaxy.

4.1.2 Global Kinematic Misalignments between Stars and Gas

Fig. 6 presents the global gaseous versus stellar kinematic PAs and the distribution of kinematic misalignments between the stellar and gaseous components in our sample. Most galaxies in our sample follow the simple one-to-one relation (left panel). Five Seyfert galaxies show an absolute misalignment larger than 20°, and for all the inactive galaxies, the misalignment between gaseous and stellar kinematic major-axes is less than 20°. Among the 5 Seyfert galaxies with strong kinematic misalignments, two are Seyfert 1 galaxies (NGC 3227 and NGC 4051) for which the BLR is detected and one is NGC 5194 which presents an outflow structure in the gaseous maps on the Northern side (Fig 4g). The other two galaxies are NGC 2655 and NGC 4579. NGC 2655 is known to host off-planar gas in the central regions (Erwin & Sparke 2003) and an inner molecular spiral is present in the nuclear region of NGC 4579 (García-Burillo et al. 2005), a spiral-like structure is also observed in our ionised gas distribution maps (Fig. 4f). In order to take out any influence of the AGN itself on the result of our analysis, we masked the BLR for the Seyfert 1 galaxies and the prominent outflow region of NGC 5194 in the stellar and gaseous velocity fields. Then we determined new values for the kinematic position angles of the stars and gas. These values of the kinematic misalignment are listed in Table 3 for these four galaxies, and we show them as non filled red diamonds in the right panel of Fig. 6. These new values are different from the PAs determined without masking the regions where the dynamics is dominated by the AGN. For NGC 4151 and NGC 5194, the kinematic misalignment between the stellar and ionised components is smaller after masking such regions. However, it is the opposite effect for NGC 4051: the difference between the stellar and gaseous kinematic major-axis orientation is larger after masking the BLR. For NGC 3227, there is no significant difference between the two values. After this second analysis, the same five Seyfert galaxies have still kinematic misalignments larger than 20°.

Although about half of our Seyferts sample presents strong misalignments between stellar and gaseous kinematics while none of the inactive galaxies shows such differences, no statistically-significant difference is found between Seyfert and control-galaxies. A Mann-Whitney U test shows that the two distributions are identical. By symmetrizing the velocity fields to look for global differences in disc orientation, this zeroth order analysis shows that our sample size is too small to be able to separate statistically the two distributions of Seyfert and inactive galaxies, despite the fact

Pairs	Name NGC	Activity	PA_{phot} (deg)	Ref	PA_{stars} (deg)	PA_{gas} (deg)	$\Delta PA_{phot-kin}$ (deg)	ΔPA_{kin} (deg)
(1)	(2)	(3)	(4)	(5)	(6)	(7)	(8)	(9)
	1068	S2	-100±5	1	-88±1	-97±1	12±6	9±2
	3227	S1	158±2	2	160±5	184±1	2±7	24±6
1	2655	S2	-95±5	3	-94±1	-174±1	1±6	80±2
	4459	inactive	-77±2	3	-80±1	-81±1	3±3	1±2
2	3627	S2	-175±5	3	-168±1	-167±1	7±6	1±2
	5806	inactive	172±2	3	171±2	157±1	1±4	14±3
3	4051	S1	-45	4	-47±3	-54±1	6±3	7±4
	5248	inactive	110±2	3	115±2	130±1	5±4	15±3
4	4151	S1	22	5	19±3	43±1	1±3	24±4
	2985	inactive	-3±1	3	-2±2	-3±1	1±3	1±3
5	4579	S2	96±2	3	99±1	154±1	3±5	55±2
	3351	inactive	-168±2	3	-164±1	-154±1	6±3	10±2
6	5194	S2	-190	6	-165±5	-134±1	25±2	30±6
	5055	inactive	102±2	3	99±1	106±1	3±4	7±2
7	6951	S2	137	7	145±2	142±1	7±3	3±3
	5248	inactive	110±2	3	115±2	130±1	5±4	15±3

Table 3. Results of the kinematic analysis of the stellar and gaseous components. (1): Pair identifier; (2): NGC number; (3): Activity; (4): Photometric position angle (PA) in degrees. The values for NGC 4151 and NGC 5194 correspond to the line of nodes PA. (5): Origin of the values for the photometric PA: 1: Emsellem et al. (2006), 2: Mundell et al. (1995), 3: R-Band DSS images ellipse fitting, 4: Christopoulou et al. (1997), 5: Pedlar et al. (1992), 6: Tully (1974), 7: Rozas et al. (2002); (6): Stellar Kinematic position angle (PA), in degrees; (7): Gas Kinematic position angle (PA), in degrees; (8): Difference between the photometric and the stellar kinematic PAs, in degrees $\Delta PA_{phot-kin} = |PA_{phot} - PA_{stars}|$; (9): Difference between the stars and gas kinematic PAs, in degrees $\Delta PA_{kin} = |PA_{stars} - PA_{gas}|$.

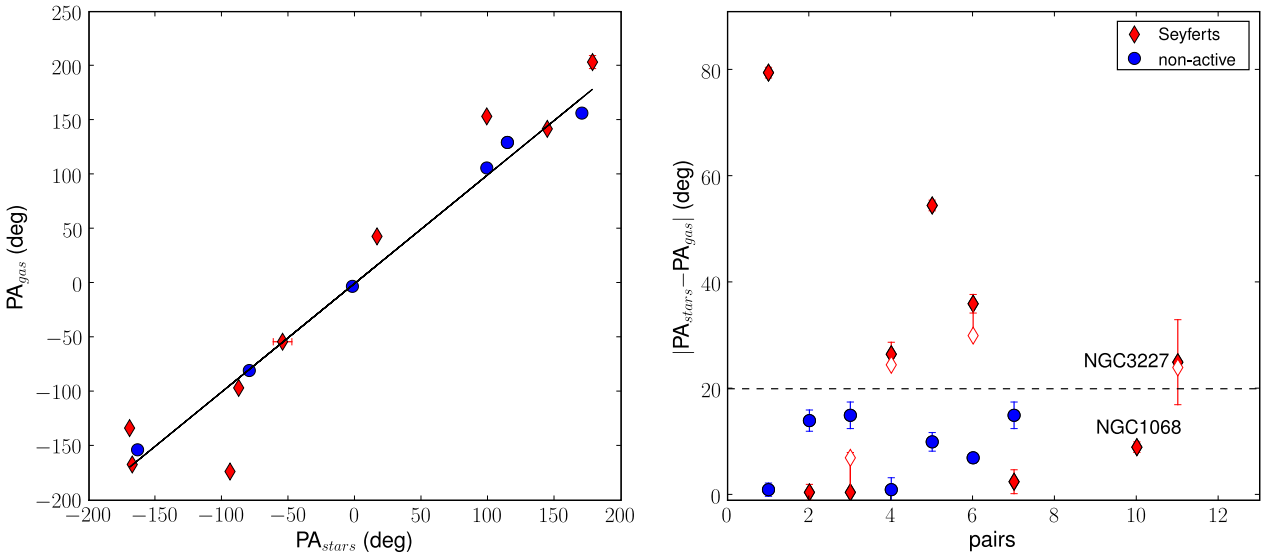


Figure 6. Kinematic misalignments between stars and gas. Left panel: global gaseous versus stellar kinematic PAs. The one-to-one relation is shown as a black line, active galaxies and inactive galaxies are shown as filled red diamonds and filled blue circles respectively. Right panel: distribution of differences of global kinematics PAs of stars and gas $PA_{stars} - PA_{gas}$ for each pair of galaxies, Seyfert (red diamonds) and inactive galaxies (blue circles). The non-filled red diamonds correspond to the PA derived by masking the BLR of the Seyfert 1 galaxies NGC 3227, NGC 4051 (pair 3) and NGC 4151 (pair 4) and the outflow bubble region for NGC 5194 (pair 6). The dashed black horizontal line corresponds to a kinematic misalignment of 20°.

that half of the Seyferts present kinematic misalignments larger than 20°.

4.2 Radial Variations of Kinematic Properties

In the above analysis, global parameters were extracted from the two-dimensional data, and therefore details of the observed kinematic structures and small-scales variations of the PA are not accounted for. Since we have the full two-dimensional dynamical information, we can analyse the stellar and ionised gas velocity fields quantitatively over the SAURON FOV and then study the kinematic properties as a function of radius. Fourier expansion of the velocity field along ellipses is a powerful technique to unveil the kinematic perturbations and therefore to give information on the gravitational potential (Schoenmakers et al. 1997; Wong et al. 2004; Krajnović et al. 2006). This formalism will be used in a second paper (Dumas et al. in preparation) on our SAURON data associated with large scale radio data obtained with the Very Large Array (VLA). For the current paper, we estimate the kinematic parameters of our stellar and gaseous velocity fields by modeling the galactic disc as a two-dimensional thin disc, in pure circular rotation with no vertical velocities. The line-of-sight velocities can then be written as:

$$\begin{aligned} V_{los}(R,\Phi,i) = V_{sys} &+ V_{rot}(R)\cos\Phi\sin i \\ &+ V_{rad}(R)\sin\Phi\sin i \end{aligned} \quad (1)$$

where V_{sys} is the systemic velocity of the galaxy, V_{rot} and V_{rad} are the rotational and radial velocities in the galactic plane. They depend only on the radius R. The disc inclination i ranges from 0° (face on) to 90° (edge on). Finally, the polar coordinates in the plane of the galaxy (R,Φ) are related to the observable coordinates (x,y) on the sky plane by:

$$\begin{cases} \cos\Phi = \dfrac{-(x-X_c)\sin\Phi_0 + (y-Y_c)\cos\Phi_0}{R} \\ \\ \sin\Phi = \dfrac{-(x-X_c)\cos\Phi_0 - (y-Y_c)\sin\Phi_0}{R\cos i} \end{cases} \quad (2)$$

(X_c, Y_c) are the coordinates of the dynamic centre and Φ_0 is the PA of the projected major-axis of the disc measured with respect to North (counter-clockwise).

We use the expression of the velocity (Eq. 1) with the tilted-ring method in order to derive the stellar and gaseous kinematic parameters. Our technique is inspired from the ROTCUR routine in the GIPSY package (Begeman 1987). The galactic disc is divided into concentric ellipses determined by 6 parameters : the centre (X_c, Y_c), position angle Φ_0, inclination i, the offset velocity V_{sys} and the rotational velocity V_{rot}. For this first iteration, V_{rad} is set to 0. The width of each ring is chosen to be large enough to have a sufficiently high number of pixels so the fit is good, and small enough to assume the rotational velocity is constant along the ring. The width of the rings is finally chosen to be equal to the seeing. All these parameters (except V_{rad}) are adjusted iteratively for each ring, by fitting the expression of the line-of-sight velocity of Eq. 1 to the observed velocity field:

(i) Initial values for V_{sys}, Φ_0 and i were taken from previous published studies or the NASA Extragalactic Database (NED). We fixed the dynamical centre to coincide with the photometric centre, or with the location of the central radio continuum peak for the Seyfert galaxies.

(ii) A first fit is done, by fixing Φ_0 and i while allowing V_{sys}, (X_c, Y_c) and V_{rot} to vary as a function of R. The mean values of V_{sys}, X_c and Y_c were taken as improved estimates for the systemic velocity and the dynamical center of the galaxy.

(iii) Then, we fit the position angle Φ_0 and V_{rot} with V_{sys} and (X_c, Y_c) fixed at the values derived from the previous step, and the disc inclination fixed at its initial guess

These three steps were followed for the stellar velocity fields of our sample. For the gaseous velocity fields, we imported the values of V_{sys} and (X_c, Y_c) derived from the first step of the fit applied on the stellar components. Then we fitted the PA and the rotational velocity as for the stars. For the Seyfert 1 galaxies and for NGC 1068, the central few arcseconds were excluded since they are highly contaminated with emission from the active nucleus (BLR or NLR).

The results of this analysis are presented in Figs. 7a and 7b. The stellar and gaseous kinematic PAs are plotted as a function of radius. The values of the global stellar and gaseous kinematic PAs derived in Sec. 4.1 are indicated on each plot as a dotted red and dashed blue lines, respectively. All angles are given relative to the photometric major-axis PA. These plots reveal the change of orientation of the stellar and gaseous kinematic major-axis orientation as a function of radius. The global values of the kinematic PAs derived in the Sec 4.1 correspond only to a small part of the FOV on which the kinematic orientation is globally constant. For NGC 3627, the global stellar and gaseous kinematic PAs derived in the previous Section correspond to values outside $R \gtrsim 15''$ (Fig. 7a), and for NGC 5806, our first method is not sensitive to the variations of PAs between 10 and 15″ (Fig. 7a). In the case of NGC 2655, the kinematic PA of the ionised gas rises abruptly for $r < 10''$ from the value found by our global method to a value close to the stellar kinematic PA.

In order to quantify the variations in the radial profiles of the kinematic PAs, we have used the difference between the maximum and minimum values of the kinematic PAs. For each galaxy, the quantity ΔPA=PA$_{max}$-PA$_{min}$ is computed for the gaseous and stellar components. To compare the Seyfert hosts to their associated inactive galaxies, the maximum and minimum values of the kinematic PAs were derived on regions corresponding to the same spatial length for the two galaxies in each pair. If the velocity fields of the Seyfert and its associated inactive galaxies extend outside $r = 1.5$ kpc, ΔPA is derived inside this radius. If one or both of the paired galaxies extend less that 1.5 kpc, the minimum radius value of the two galaxies is used. The central few arcseconds where residual AGN-induced perturbations may be present are excluded. The resulting ΔPA values for both the gaseous and stellar components, and for all galaxies in our sample (Seyfert and inactive) are provided in Fig. 8. Also shown is the *average* ΔPA of each component for the inactive galaxies (blue lines) and the Seyfert galaxies (red lines). For the latter, the average is made excluding NGC 1068 and NGC 3227 since these two Seyfert do not have associated control galaxies.

The first result of this analysis comes from a compar-

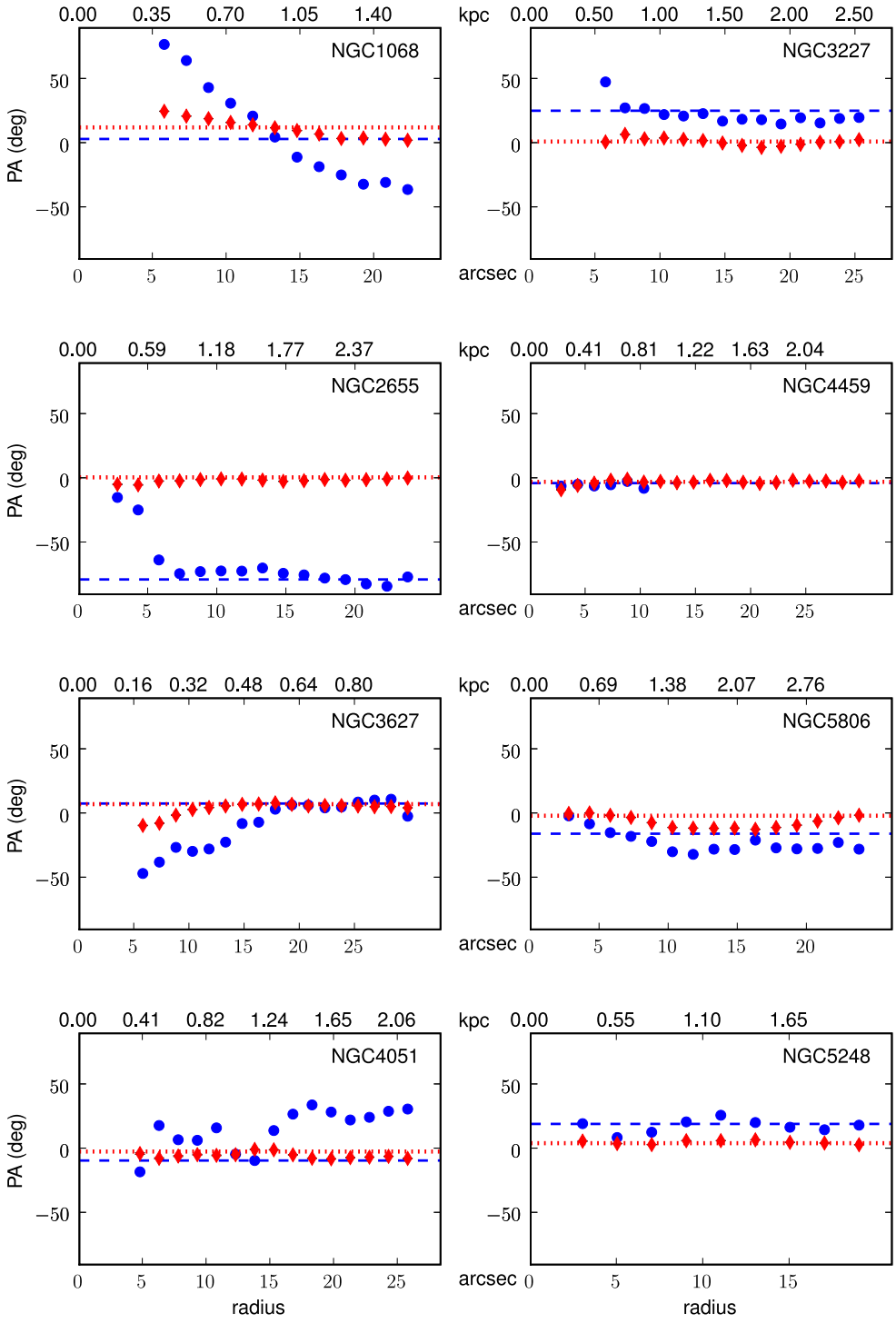


Figure 7a. Kinematic position angles of the stars (red diamonds) and of the gas (blue circles) components as a function of radius. The first row shows the Seyfert galaxies NGC 1068, and NGC 3227. Each subsequent row presents a pair of galaxies: the Seyfert on the left, and the inactive galaxy on the right. The regions related to the BLR of the Seyfert 1 galaxies (NGC 3227, NGC 4051 and NGC 4151) and to the NLR of NGC 1068 have been excluded from the fit. The dotted red and dashed blue horizontal lines represent the values of the global position angle of the kinematic major-axis for the stars and gas respectively. These values were derived from the velocity field symmetrization method (see Section 4.1). The values are relative to the photometric PA (see Table 3).

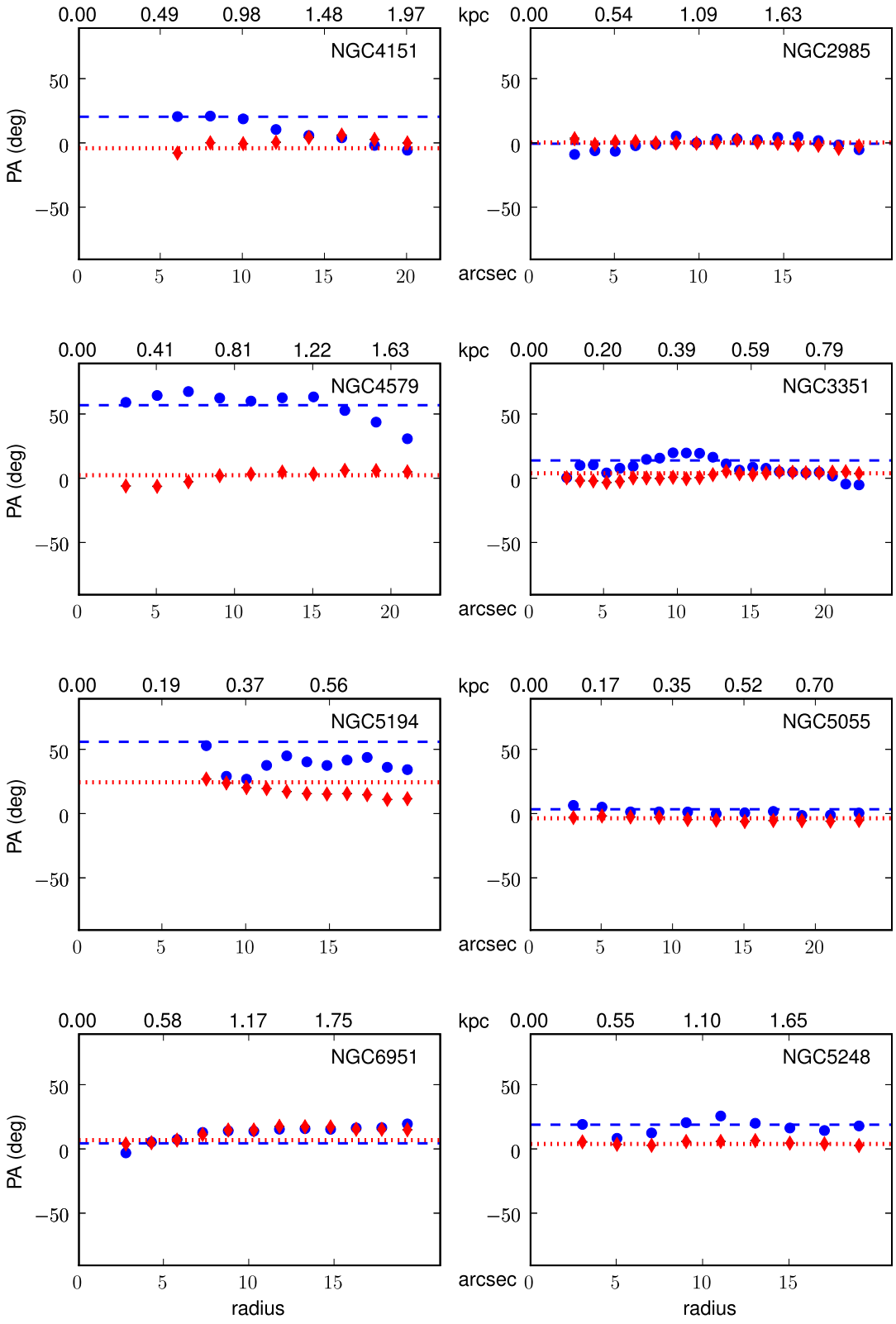


Figure 7b. Fig. 7a continued.

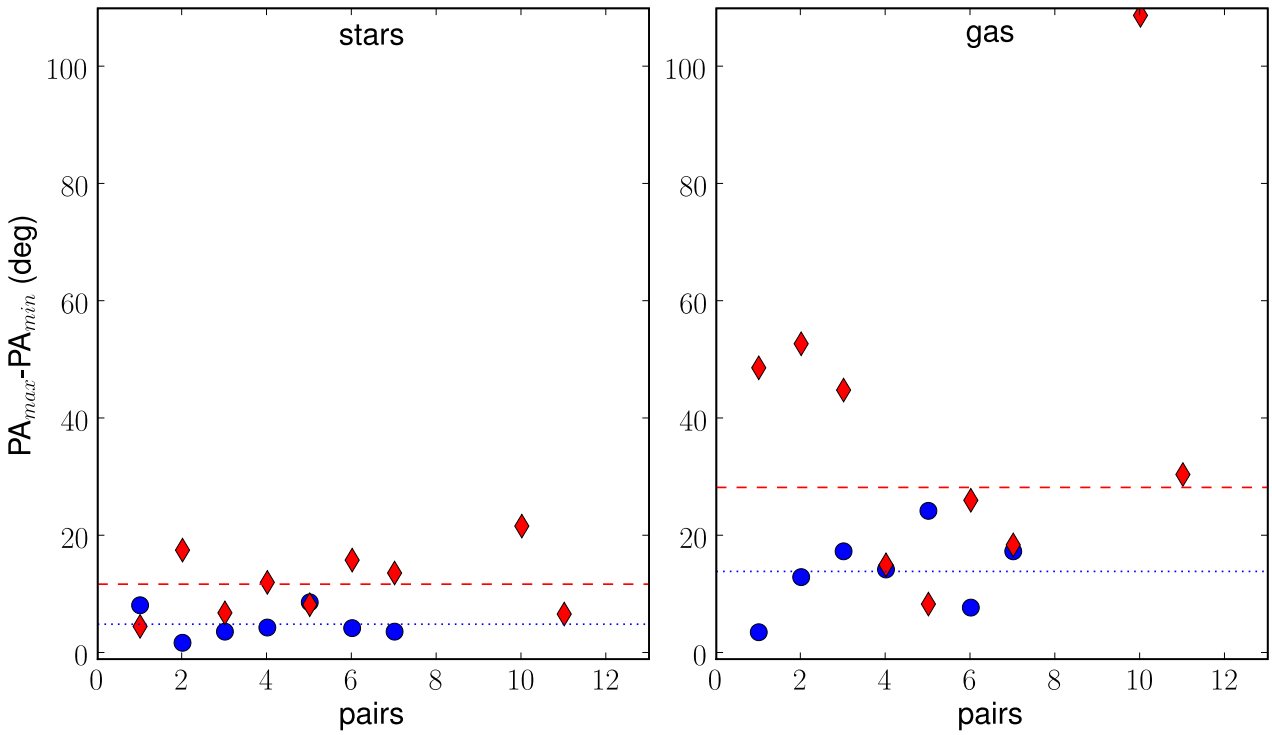


Figure 8. Distribution of the amplitude of variations of the stellar (left panel) and the gaseous (right panel) kinematic PAs in the inner 1.5 kpc (see text for details). Active galaxies and inactive galaxies are shown as filled red diamonds and filled blue circles respectively. The dotted blue and dashed red lines correspond to the average of PA$_{max}$-PA$_{min}$ for the inactive and Seyfert galaxies respectively, for the stellar (left panel) or gaseous (right panel) components. NGC 1068 and NGC 3227 have been excluded to compute the average values corresponding to the Seyfert galaxies, since they do not have an associated inactive galaxy.

ison between the gaseous and stellar components: for both the Seyfert and inactive sub-samples, ΔPA is almost always higher for the gas than for the stars. While the stellar kinematic PAs radial variations are restrained within about 10° and 20° for the inactive and Seyfert galaxies, respectively, such variations of the gaseous PAs reach more than 40° in the case of four Seyfert galaxies (NGC 1068, NGC 2655 and NGC 3627 and NGC 4051). The average ΔPA of the gaseous component is about ∼ 3 times greater than the average ΔPA of the stars for the Seyfert galaxies as well as for the inactive galaxies. The second result is obtained when comparing the Seyfert and inactive galaxies: for both gas and stars, ΔPA is almost always larger for the Seyferts than for their control inactive galaxies. The average ΔPA for the Seyferts is about 2.5 times greater than the average ΔPA for the inactive galaxies, considering either the stellar or the ionised gas components.

5 DISCUSSION AND CONCLUSION

5.1 Accretion Rates and Kinematic Misalignments

In this section we highlight the relationship between kinematic disturbances in the galaxy and the accretion rate of the nuclear black hole. Throughout this paper we use the nuclear type classification of Ho et al. (1997). Figure 9 presents our galaxies in the diagnostic diagram Log([O III]λ5007/Hβ)

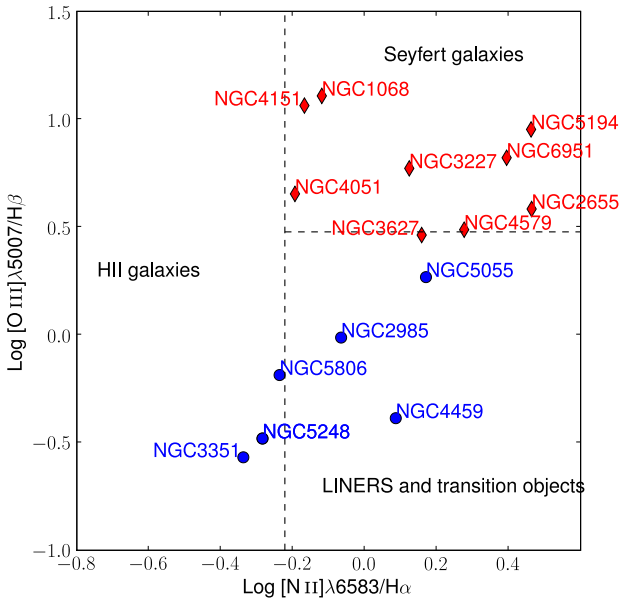


Figure 9. Diagnostic diagram for the galaxies of our sample, Log([O III]λ5007/Hβ) vs Log([N II]λ6583/Hα). The emission line ratios are from Ho et al. (1997). Active galaxies are shown as filled red diamonds and inactive galaxies as filled blue circles. Finally, the classification boundaries from Ho et al. (1997) are shown as black dashed lines.

vs Log([N II]λ6583/Hα), as well as the boundaries between the different excitation classes adopted by Ho et al. (1997). The separation between Seyfert and LINERS objects is not as sharp as depicted by this diagnostic diagram. We can notice that NGC 5055 is close to be a Seyfert while NGC 3627 and NGC 4579 are Seyferts and close to the LINERS and Transition objects. The activity classification of the sample nuclei therefore does not necessarily accurately represent the nuclear black hole accretion rate. We have then estimated the Eddington rates and the corresponding mass accretion rates of the individual nuclei from four relatively independent methods. The results are summarized in Table 4. The Black Hole masses in this Table (column 3) are from direct dynamic measurements (e.g. NGC 1068), from reverberation mapping results (e.g. NGC 4051, NGC 4151), or estimated from the central stellar velocity dispersion in our SAURON maps via the well-studied M-σ relationship (e.g. Tremaine et al. 2002). We have used four observational estimates for the Eddington ratio of the nuclei. The first is the optical continuum luminosity of the galaxy nucleus from HST images (column 4 of Table4), interpreted as optical synchrotron radiation from the base of the jet (Chiaberge et al. 2005). No bolometric correction is applied so the result should be considered a lower limit to the Eddington ratio. Of course, contamination of the nuclear optical continuum from star formation could cause the AGN-related luminosity value to be lower. We have also used the hard (2–10 keV) X-ray luminosity, the nuclear [O III] luminosity (from Panessa et al. 2006 and Ho et al. 1997) and the nuclear radio power to estimate the bolometric luminosity of the nucleus (columns 5 to 7 of Table 4). In the case of the [O III] luminosity, we tested the estimator used for active galaxies in the SDSS – $L_{bol} = 3500 \times L_{[O\,III]}$ (Heckman et al. 2004). This formula resulted in too high values of L_{bol} for our sample. The factor 3500 derived by Heckman et al. (2004) was based on the empirically derived ratios $L_{5000}/L_{[O\,III]} = 320$, where L_{5000} is the monochromatic continuum luminosity λP_λ at 5000Åand $L_{bol}/L_{5000} = 10.9$. Heckman et al. (2004) based and tested this relationship mainly on AGN with Log [O III] luminosities of 6.5 and above. Our sample has much lower Log [O III] luminosities, ranging from 3.8 to 8.3, with median value 5.1. We find that a factor of 90, instead of 3500, gives a more reasonable value for the bolometric luminosity within our sample. This lower factor could reflect a higher [O III] emission relative to L_{5000} from our lower luminosity, gas rich systems as compared to the SDSS Seyferts. In the case of nuclear radio luminosities, we used the sub-arcsecond AGN-related radio flux to calculate the implied jet mechanical power (see Nagar et al. 2005 for details). Nagar et al. (2005) have demonstrated that this method to calculate the bolometric luminosity works well in low luminosity AGN. For each nucleus, we then adopted a value of $l_{Edd} = L_{bol}/L_{Edd}$ (column 8 of Table 4) from the previous four values, keeping in mind their relative uncertainties and the paradigm that low luminosity AGNs in the low (high) state are more likely to produce radio (X-ray) emission. This adopted value of the Eddington ratio was used to calculate the estimated mass accretion rate (column 9). The 'inactive' galaxies NGC 3351, NGC 5248, and NGC 5806, all three with HII-type nuclei, have not been detected in the hard X-ray nor radio. Their Eddington ratios are likely lower than the value adopted in Table 4, since a significant part of their nuclear [O III] luminosity could come from HII regions. Note that while the overall 'Seyfert' and 'inactive' samples show expectedly different Eddington ratios, there is some overlap; two of the Seyferts, NGC 3627 and NGC 6951, have Eddington ratios similar to the inactive nuclei.

The relationship between mass accretion rate and the kinematic of the gas and stars is illustrated in Fig. 10. The result is rather striking: black holes with low accretion rates reside in galaxies in which the stellar and gas kinematic axes are closely aligned and in which the gas kinematic axis is least disturbed, while Black holes with accretion rates higher than $10^{-4.5}$ $M_\odot$/yr reside in galaxies with either either a large misalignment between gas and stellar axes, or a large twist in their gas kinematic axes.

5.2 Feeding the AGN

Why a fraction of nearby galaxies host an active nucleus still remains an unsolved question. Several mechanisms may be involved in the fueling of the central regions of galaxies, and subsequently activating and sustaining nuclear activity. Removal of angular momentum and transportation of the gas towards the very central region may be driven by gravitational perturbations due to interactions such as mergers of galaxies or tidal interaction (Barnes & Hernquist 1991, 1996), or non-axisymmetric galactic structures (Shlosman et al. 2000, e.g. bars, spirals,), as well as turbulence instabilities and shocks in the interstellar medium. The majority of optical and near infra-red (NIR) imaging studies failed to find any morphological difference between active and inactive galaxies on a range of scales that encompasses galactic interactions, stellar bars and nuclear spirals (Martini et al. 2003; Knapen et al. 2000; Márquez et al. 2000). However, Hunt & Malkan (2004) found significant excess of isophotal twists and morphological disturbances in Seyfert 2 galaxies compared to inactive and Seyfert 1 or LINER galaxies. Another recent study of the presence and structures of dust in the circumnuclear regions revealed differences between early type Seyfert and inactive galaxies (Simões Lopes et al. 2007). These results suggest the possibility of identifiable dynamical differences, in the circumnuclear regions in active and inactive galaxies.

In this study, we investigated the stellar and ionised gas kinematics of a well-defined sample of nearby active and inactive galaxies, in order to probe the galactic potential in the central kpc regions. First, we have measured the kinematic misalignments between the stellar and the ionised components. The distribution of kinematic misalignments has often been used to constrain the origin of the ionised gas in early-type galaxies (Bertola et al. 1992; Sarzi et al. 2006). If the gas is produced internally (e.g. stellar mass loss) and comes from the galactic disc, the bulk of the gaseous component in the central region is expected to co-rotate with the stars. The angular momenta of the stellar and gaseous components would therefore be globally aligned. Some mild misalignments may exist due to the effect of non-axisymmetric structures (bars, spirals), or the presence of decoupled stellar components. Gas acquired from an external source, e.g. via interaction with galaxies or the intergalactic medium, should eventually settle in the existing principal planes of the gravitational potential. In a triaxial potential hosting a large-

Pairs	Name NGC	Log $M_\bullet$ ($M_\odot$)	Log L_{opt}/L_{Edd} (HST)	Log L_{bol}/L_{Edd} (X-ray)	Log L_{bol}/L_{Edd} ([O III])	Log L_{bol}/L_{Edd} (Radio)	Log L_{bol}/L_{Edd} (Adopted)	Log $\dot{m}$ ($M_\odot$/yr)
(1)	(2)	(3)	(4)	(5)	(6)	(7)	(8)	(9)
	1068	6.90	···	-1.3	-1.1	-1.6	-1.3	-2.0
	3227	7.59	-3.8	-3.1	-3.2	-3.5	-3.3	-3.4
1	2655	8.14	···	-3.6	-4.4	-3.8	-3.6	-3.1
	4459	7.81	···	-6.2	-6.1	<-4.3	-6.2	-6.0
2	3627	7.22	···	<-6.6	-4.6	-4.3	-5.5	-5.9
	5806	7.07	···	···	-4.9	···	-4.9	-5.5
3	4051	6.11	-2.8	-2.1	-2.4	<-2.4	-2.3	-3.8
	5248	7.27	···	···	-5.4	···	-5.4	-5.8
4	4151	7.18	-2.1	-2.0	-1.9	-2.6	-2.2	-2.7
	2985	7.76	···	···	-5.9	<-4.1	-5.9	-5.8
5	4579	7.79	···	-4.0	-4.5	-3.2	-3.8	-3.7
	3351	7.13	···	···	-5.9	···	-5.9	-6.4
6	5194	6.34	···	-2.7	-2.6	<-3.1	-2.8	-4.1
	5055	7.06	···	-6.0	-5.1	<-4.0	-5.8	-6.4
7	6951	7.47	···	-5.1	-4.9	<-3.6	-5.0	-5.2
	5248	7.27	···	···	-5.4	···	-5.4	-5.8

Table 4. Eddington Ratios and Mass Accretion Rates. Columns are: (1) Pair; (2) Galaxy name; (3) Black Hole mass from Lodato & Bertin (2003) (NGC 1068, maser dynamics), Kaspi et al. (2000) (NGC 3227, NGC 4051, NGC 4151; reverberation mapping), Sarzi et al. (2001) (NGC 4459). For the other galaxies, we estimated the black hole mass from the average stellar σ in the central $10''$ of our SAURON maps using the Tremaine et al. (2002) relationship; (4) ratio of nuclear (HST) optical luminosity (with no bolometric correction applied; from Chiaberge et al. 2005) to Eddington luminosity; (5) Eddington ratio derived from the 2-10 keV X-ray luminosity, using the emperical relation found by Ulvestad & Ho (2001): $L_{bol} = 6.7\ L_X$(2-10 keV). The data are from the compilation in Panessa et al. (2006), except for NGC 4459 and NGC 5055 (González-Martín et al. 2006) and NGC 6951 (Kim et al. 1992; from *Einstein* data with no correction applied to transform the luminosity to the 2–10 keV regime); (6) Eddington ratio derived from the [O III] luminosity using $L_{bol} = 90 * L_{[O\,III]}$ (see text); (7) Eddington ratio implied by the mechanical energy in the radio jet (Q_{jet}) as derived from the nuclear radio emission (see Nagar et al. 2005); (8) adopted Eddington ratio: this was roughly calculated from columns 3 to 6 keeping in mind the reliability of the various values; (9) the mass accretion rate implied by the adopted Eddington ratio under the standard assumption of a 10% radiative efficiency for the accretion process.

scale disc, the gas would thus preferentially fall onto either the disc equatorial plane or in a plane perpendicular to it, giving rise to a polar ring. Polar rings are observed in a few nearby early-type galaxies (see e.g. Bertola et al. 1992). The distribution of kinematic misalignments, measured as position angle differences between kinematic major-axes, around the reference values of 0, 90 and 180°, should therefore be closely linked with the origin of the accreted gas.

So far, there seems to be no trend for the kinematic misalignments of early-type galaxies with respect to Hubble type, galactic environment and galaxy luminosity (Sarzi et al. 2006). In our sample, five Seyfert galaxies present significant kinematic misalignments (>20°) however, only NGC 2655 presents a gaseous component rotating almost perpendicularly to the stellar component. For all the other Seyfert (four objects) and for all the inactive galaxies, the ionised gas co-rotates with the stars (kinematic misalignments smaller than 20°). This follows the results of Sarzi et al. (2006) for a sample of later-type galaxies and therefore suggests that the presently observed ionised gas in the circumnuclear regions does not have a purely external origin for both the Seyfert and the inactive galaxies. The only clear exception is NGC 2655, a galaxy known to host a polar ring (Keel & Hummel 1988). It is interacting with a companion and had presumably suffered a minor merger in the past (Huchtmeier & Richter 1982). Interaction between galaxies is an efficient way to transport gas towards the central parts and to trigger nuclear star formation (Barnes & Hernquist 1991), but it seems neither a necessary nor a sufficient mechanism for most Seyfert activity (De Robertis et al. 1998; Schmitt 2001; Ho et al. 2003).

A more refined analysis revealed that the radial variations of the kinematic PAs of the ionised gas are three times greater for the Seyfert than for their associated inactive galaxies, in the central 1.5 kpc. Indeed, due to the relatively large pixel size of SAURON compared with other IFUs and the conservative approach of our analysis, the intrinsic gaseous deviations may be even larger than suggested by our results, particularly for the very inner regions. Although our sample is small, this trend hints for the presence of non-axisymmetric perturbations of the gravitational potential in the inner kpc of the Seyfert galaxies. Since the observed stellar velocity fields of these active galaxies are very regular with major axes rather well aligned with the outer photometric ones, theses dynamical perturbations must be small. The gas, being more sensitive to small deviations from axisymmetry, responds better to small non-axisymmetric structures such as weak bars or spirals. This would be in fact in agreement with previous imaging studies which found no strong excess of bars or nuclear spirals in

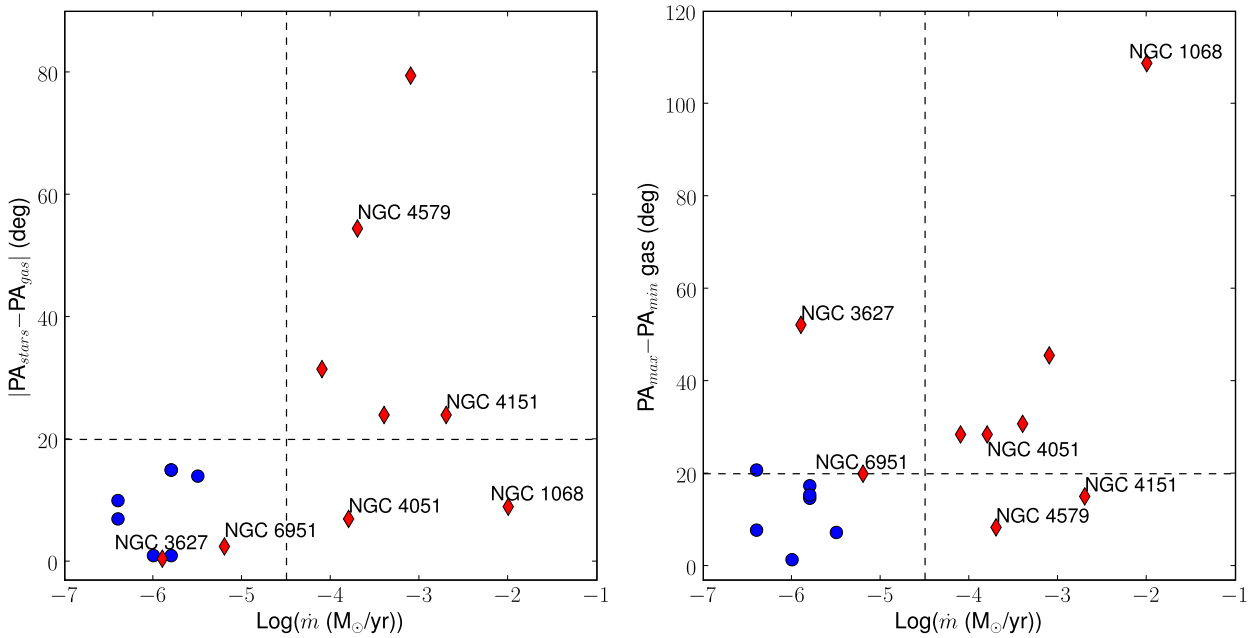


Figure 10. Distribution of the differences between the global kinematic PAs of the stars and gas (left panel) and the amplitude of variations of the gaseous kinematic PAs in the inner 1.5kpc (right panel) as a function of the mass accretion rate (see Table 4). Active galaxies are shown as filled red diamonds and inactive galaxies as filled blue circles. For reference, a line is drawn at ΔPA=20° and mass accretion rate = $10^{-4.5}$ M$_\odot$/yr in each of the panels.

Seyfert galaxies. If strong deviations from axial symmetric were present, the gaseous kinematics would have been extremely disturbed and easily detectable with standard (long-slit) spectroscopy techniques. The presence of weak deviations from axial symmetry in Seyfert galaxies seems to be in good agreement with the refined imaging study of Hunt & Malkan (2004). They found an excess of NIR isophotal twists in Seyfert 2 hosts compared to inactive galaxies, and discussed the non-axisymmetric instabilities (nuclear disc, nested misaligned bars, triaxial structures) which could be responsible for such morphological perturbations. This excess of isophotal twist is not observed for the Seyfert 1 galaxies, Hunt & Malkan (2004) interpreted this difference between Seyfert 1 and Seyfert 2 galaxies as an evolutionary effect, the Seyfert 1 hosts being 'older' than the Seyfert 2 ones in their scenario. We would need a larger sample to investigate statistical differences in the ionised gas properties of Seyfert 1 and 2 galaxies. A larger study of Active vs. Inactive galaxies in the SDSS with IMACS is now in progress within our group, the active and inactive galaxies drawn from the same parent sample so hopefully reducing any underlying selection biases and also offering more controls per Seyfert (Westoby et al. in preparation).

In addition to a ready supply of fuel and a transportation mechanism, timescales are important. Galaxies are thought to experience recurrent episodes of nuclear activity in their lifetime, with instabilities in the fueling rate possibly regulating the activity cycles (Saripalli & Mack 2007). Dynamical instabilities in the inner kpc regions and nuclear activity can evolve in parallel. However, due to the time required to set up sufficient gas inflow, the non-axisymmetric perturbations may be observed while not enough gas has been driven in the vicinity of the SMBH and the galaxy is inactive. Similarly such gravitational instabilities may have disappeared when the nuclear activity is still underway. Observationally, it is therefore reasonable to hypothesise that a snapshot of active and inactive galaxies might show equal degrees of host galaxy disturbance. However, while disturbed gas observed in a host galaxy is not the gas that is simultaneously fueling the nuclear activity, the dynamical time scale in the circumnuclear regions is similar to the AGN lifetime. Therefore, the correlation between the presence of perturbation in the ionised gas in the central kpc regions and the nuclear activity suggested by our study is striking and supports a close link between the AGN, host dynamics on scales of hundreds to tens of parcsecs and relevant dynamical and activity timescales.

Finally, the presence of σ-drops in the stellar velocity fields observed for some of our galaxies may indicate the presence of cold nuclear stellar discs (Emsellem et al. 2001). Wozniak et al. (2003) interpreted such structures as the result of star formation following the accretion of gas in the central few hundred parsecs. High resolution follow-up IFU mapping of the central few arcseconds, using e.g. the OASIS IFU, could reveal direct evidence for these discs. Such data on a relatively small FOV are rather difficult to interpret. However, associated with our larger scale SAURON maps, they could extend our understanding of fuel delivery closer again to the AGN.

5.3 Summary

In this paper, we have presented two dimensional morphology and kinematic maps of the stars and ionised gas compo-

nent in the central kpc regions of a distance limited sample of well-matched Seyfert and non-Seyfert galaxies. We found that:

• Kinematics of the stellar and gaseous components in the circumnuclear regions of our galaxies are dominated by disc-like rotation. The stellar kinematics present very regular rotation patterns for both inactive and Seyfert galaxies in agreement with previous studies (Barbosa et al. 2006). Ionised gas is generally co-rotating with respect to the stars.

• The stellar global kinematic major-axes are aligned within 10° with the outer galactic disc major-axis for all galaxies, except for two Seyferts: NGC 1068 and NGC 5194, for which the determination of the photometric major axis orientation is quite uncertain. Except for these two particular galaxies, the circumnuclear stellar kinematic major axis is a robust determination of the line-of-nodes for either the Seyfert and the non-active galaxies.

• The gaseous component co-rotates with the stars, the global stellar and gaseous kinematic PAs being aligned for all galaxies within 20°, except for two Seyfert galaxies: NGC 2655 and NGC 4579. Our kinematic maps reveal some disturbances in the gaseous velocity field, which may be evidence for deviations from axisymmetry. These perturbations in the ionised velocity fields may hint for the presence of streaming or radial flows, which could be related to fueling mechanisms.

• The gaseous kinematics PAs have radial variations over the SAURON FOV 3 times greater than the stellar ones, for either the Seyfert and their associated inactive galaxies.

• The variations of the stellar and gaseous PAs in the central kpc of the Seyfert galaxies are 2.5 times greater than those of the inactive galaxies.

We conclude that the increased incidence of disturbed ionised gas in the circumnuclear regions of the Seyferts on scales of hundreds to tens of parsecs, compared with inactive galaxies, supports a close link between nuclear host dynamics and relevant dynamical and activity timescales.

ACKNOWLEDGMENTS

We thank Michele Cappellari for the IDL implementation of the position angles routine. We would like to warmly thank Pierre Ferruit and Bruno Jungwiert for their contribution and fruitful discussions at an early stage of this project, and we thank Tim de Zeeuw and the referee, Jack Gallimore, for useful comments that improved the paper. CGM acknowledges financial support from the Royal Society. The SAURON-related projects are made possible through grants 614.13.003, 781.74.203, 614.000.301 and 614.031.015 from NWO and financial contributions from the Institut National des Sciences de l'Univers, the Université Claude Bernard de Lyon I, the Universities of Durham, Leiden and the Netherlands Research School for Astronomy NOVA. The SAURON observations were obtained at the William Herschel Telescope, operated by the Isaac Newton Group in the Spanish Observatorio del Roque de los Muchachos of the Instituto de Astofísica de Canarias. We would also like to thank the WHT staff for their technical support at the telescope. This work made use of the HyperLeda and the NED databases. Part of this work is based on data obtained from the STSci Science Archive Facility. The Digitized Sky Surveys were produced at the Space Telescope Science Institute under US Government grant NAG W-2166. The images of these surveys are based on photographic data obtained using the Oschin Schmidt Telescope on Palomar Mountain and the UK Schmidt Telescope

REFERENCES

Afanasiev V. L., Sil'chenko O. K., 2005, A & A, 429, 825
Allard E. L., Knapen J. H., Peletier R. F., Sarzi M., 2006, MNRAS, 371, 1087
Antonucci R. R. J., Miller J. S., 1985, ApJ, 297, 621
Arribas S., Mediavilla E., 1994, ApJ, 437, 149
Asif M. W., Mundell C. G., Pedlar A., 2005, MNRAS, 359, 408
Asif M. W., Mundell C. G., Pedlar A., Unger S. W., Robinson A., Vila-Vilaro B., Lewis J. R., 1998, A & A, 333, 466
Bacon R., Copin Y., Monnet G., Miller B. W., Allington-Smith J. R., Bureau M., Carollo C. M., Davies R. L., Emsellem E., Kuntschner H., Peletier R. F., Verolme E. K., de Zeeuw P. T., 2001, MNRAS, 326, 23
Barbosa F. K. B., Storchi-Bergmann T., Cid Fernandes R., Winge C., Schmitt H., 2006, MNRAS, pp 777–+
Barnes J. E., Hernquist L., 1996, ApJ, 471, 115
Barnes J. E., Hernquist L. E., 1991, ApJ, 370, L65
Battaglia G., Fraternali F., Oosterloo T., Sancisi R., 2006, A & A, 447, 49
Begeman K. G., 1987, PhD thesis, , Kapteyn Institute, (1987)
Bertola F., Buson L. M., Zeilinger W. W., 1992, ApJ, 401, L79
Binney J., Tremaine S., 1987, Galactic dynamics. Princeton, NJ, Princeton University Press, 1987, 747 p.
Blais-Ouellette S., Amram P., Carignan C., Swaters R., 2004, A & A, 420, 147
Bland-Hawthorn J., Gallimore J. F., Tacconi L. J., Brinks E., Baum S. A., Antonucci R. R. J., Cecil G. N., 1997, Ap&SS, 248, 9
Cappellari M., Copin Y., 2003, MNRAS, 342, 345
Cappellari M., Emsellem E., 2004, PASP, 116, 138
Carollo C. M., Stiavelli M., Seigar M., de Zeeuw P. T., Dejonghe H., 2002, AJ, 123, 159
Chemin L., Cayatte V., Balkowski C., Marcelin M., Amram P., van Driel W., Flores H., 2003, A & A, 405, 89
Chiaberge M., Capetti A., Macchetto F. D., 2005, ApJ, 625, 716
Christopoulou P. E., Holloway A. J., Steffen W., Mundell C. G., Thean A. H. C., Goudis C. D., Meaburn J., Pedlar A., 1997, MNRAS, 284, 385
Davies R. I., Thomas J., Genzel R., Mueller Sánchez F., Tacconi L. J., Sternberg A., Eisenhauer F., Abuter R., Saglia R., Bender R., 2006, ApJ, 646, 754
De Robertis M. M., Yee H. K. C., Hayhoe K., 1998, ApJ, 496, 93
de Zeeuw P. T., Bureau M., Emsellem E., Bacon R., Carollo C. M., Copin Y., Davies R. L., Kuntschner H., Miller B. W., Monnet G., Peletier R. F., Verolme E. K., 2002, MNRAS, 329, 513
Devereux N. A., Kenney J. D., Young J. S., 1992, AJ, 103, 784

Emsellem E., Cappellari M., Peletier R. F., McDermid R. M., Bacon R., Bureau M., Copin Y., Davies R. L., Krajnović D., Kuntschner H., Miller B. W., de Zeeuw P. T., 2004, MNRAS, 352, 721
Emsellem E., Fathi K., Wozniak H., Ferruit P., Mundell C. G., Schinnerer E., 2006, MNRAS, 365, 367
Emsellem E., Greusard D., Combes F., Friedli D., Leon S., Pécontal E., Wozniak H., 2001, A & A, 368, 52
Erwin P., 2005, MNRAS, 364, 283
Erwin P., Sparke L. S., 2003, APJS, 146, 299
Falcón-Barroso J., Bacon R., Bureau M., Cappellari M., Davies R. L., de Zeeuw P. T., Emsellem E., Fathi K., Krajnović D., Kuntschner H., McDermid R. M., Peletier R. F., Sarzi M., 2006, MNRAS, 369, 529
Fathi K., van de Ven G., Peletier R. F., Emsellem E., Falcón-Barroso J., Cappellari M., de Zeeuw T., 2005, MNRAS, 364, 773
Ferrarese L., Merritt D., 2000, ApJ, 539, L9
Ferruit P., Mundell C. G., Nagar N. M., Emsellem E., Pécontal E., Wilson A. S., Schinnerer E., 2004, MNRAS, 352, 1180
Ford H. C., Crane P. C., Jacoby G. H., Lawrie D. G., van der Hulst J. M., 1985, ApJ, 293, 132
Ganda K., Falcón-Barroso J., Peletier R. F., Cappellari M., Emsellem E., McDermid R. M., de Zeeuw P. T., Carollo C. M., 2006, MNRAS, 367, 46
García-Burillo S., Combes F., Hunt L. K., Boone F., Baker A. J., Tacconi L. J., Eckart A., Neri R., Leon S., Schinnerer E., Englmaier P., 2003, A & A, 407, 485
García-Burillo S., Combes F., Schinnerer E., Boone F., Hunt L. K., 2005, A & A, 441, 1011
García-Gómez C., Athanassoula E., Barberà C., 2002, A&A, 389, 68
Garcia-Lorenzo B., Mediavilla E., Arribas S., del Burgo C., 1997, ApJ, 483, L99+
Gebhardt K., Bender R., Bower G., Dressler A., Faber S. M., Filippenko A. V., Green R., Grillmair C., Ho L. C., Kormendy J., Lauer T. R., Magorrian J., Pinkney J., Richstone D., Tremaine S., 2000, ApJ, 539, L13
Gerssen J., Allington-Smith J., Miller B. W., Turner J. E. H., Walker A., 2006, MNRAS, 365, 29
González-Martín O., Masegosa J., Márquez I., Guerrero M. A., Dultzin-Hacyan D., 2006, A & A, 460, 45
Heckman T. M., Kauffmann G., Brinchmann J., Charlot S., Tremonti C., White S. D. M., 2004, ApJ, 613, 109
Ho L. C., Filippenko A. V., Sargent W. L. W., 1997, ApJS, 112, 315
Ho L. C., Filippenko A. V., Sargent W. L. W., 2003, ApJ, 583, 159
Huchtmeier W. K., Richter O.-G., 1982, A & A, 109, 331
Hunt L. K., Malkan M. A., 2004, ApJ, 616, 707
Jogee S., Knapen J. H., Laine S., Shlosman I., Scoville N. Z., Englmaier P., 2002, ApJ, 570, L55
Jogee S., Scoville N., Kenney J. D. P., 2005, ApJ, 630, 837
Jogee S., Shlosman I., Laine S., Englmaier P., Knapen J. H., Scoville N., Wilson C. D., 2002, ApJ, 575, 156
Jourdain E., Collin S., Dennefeld M., Ballet J., Roques J. P., Lebrun F., Mandrou P., Cordier B., Finoguenov A., Churazof E., Gilfanov M., Sunyaev R., Kuleshova N., Sheikhet A., Sukhanov K., Tserenin I., 1994, A & A, 281, L57
Kaspi S., Smith P. S., Netzer H., Maoz D., Jannuzi B. T., Giveon U., 2000, ApJ, 533, 631
Kassin S. A., de Jong R. S., Pogge R. W., 2006, ApJS, 162, 80
Keel W. C., Hummel E., 1988, A & A, 194, 90
Kewley L. J., Groves B., Kauffmann G., Heckman T., 2006, MNRAS, 372, 961
Kim D.-W., Fabbiano G., Trinchieri G., 1992, ApJS, 80, 645
Knapen J. H., Shlosman I., Peletier R. F., 2000, ApJ, 529, 93
Krajnović D., Cappellari M., de Zeeuw P. T., Copin Y., 2006, MNRAS, 366, 787
Kuntschner H., Emsellem E., Bacon R., Bureau M., Cappellari M., Davies R. L., de Zeeuw P. T., Falcón-Barroso J., Krajnović D., McDermid R. M., Peletier R. F., Sarzi M., 2006, MNRAS, 369, 497
Laine S., Knapen J. H., Pérez-Ramírez D., Englmaier P., Matthias M., 2001, MNRAS, 324, 891
Laurikainen E., Salo H., Buta R., 2004, ApJ, 607, 103
Lodato G., Bertin G., 2003, A & A, 398, 517
Márquez I., Durret F., Masegosa J., Moles M., González Delgado R. M., Marrero I., Maza J., Pérez E., Roth M., 2000, A&A, 360, 431
Márquez I., Masegosa J., Durret F., González Delgado R. M., Moles M., Maza J., Pérez E., Roth M., 2003, A & A, 409, 459
Martini P., Regan M. W., Mulchaey J. S., Pogge R. W., 2003, ApJ, 589, 774
Mediavilla E., Arribas S., 1993, Nature, 365, 420
Mediavilla E., Arribas S., 1995, MNRAS, 276, 579
Mueller Sánchez F., Davies R. I., Eisenhauer F., Tacconi L. J., Genzel R., Sternberg A., 2006, A & A, 454, 481
Mulchaey J. S., Regan M. W., 1997, ApJ, 482, L135+
Mundell C. G., 2003, in Collin S., Combes F., Shlosman I., eds, ASP Conf. Ser. 290: Active Galactic Nuclei: From Central Engine to Host Galaxy The Host Galaxy-AGN Connection - Is Neutral Gas the Key?. pp 535–+
Mundell C. G., Dumas G., Schinnerer E., Nagar N., Haan S., Wilcots E., Wilson A. S., Emsellem E., Ferruit P., Peletier R. F., de Zeeuw P. T., 2007, New AR, 51, 34
Mundell C. G., Holloway A. J., Pedlar A., Meaburn J., Kukula M. J., Axon D. J., 1995, MNRAS, 275, 67
Mundell C. G., James P. A., Loiseau N., Schinnerer E., Forbes D. A., 2004, ApJ, 614, 648
Mundell C. G., Pedlar A., Axon D. J., Meaburn J., Unger S. W., 1995, MNRAS, 277, 641
Mundell C. G., Shone D. L., 1999, MNRAS, 304, 475
Mundell C. G., Wrobel J. M., Pedlar A., Gallimore J. F., 2003, ApJ, 583, 192
Muxlow T. W. B., Pedlar A., Holloway A. J., Gallimore J. F., Antonucci R. R. J., 1996, MNRAS, 278, 854
Nagar N. M., Falcke H., Wilson A. S., 2005, A & A, 435, 521
Noordermeer E., van der Hulst J. M., Sancisi R., Swaters R. A., van Albada T. S., 2005, A & A, 442, 137
Panessa F., Bassani L., Cappi M., Dadina M., Barcons X., Carrera F. J., Ho L. C., Iwasawa K., 2006, A & A, 455, 173
Pedlar A., Howley P., Axon D. J., Unger S. W., 1992, MNRAS, 259, 369
Peeples M. S., Martini P., 2006, ApJ, 652, 1097
Perez E., Gonzalez-Delgado R., Tadhunter C., Tsvetanov

Z., 1989, MNRAS, 241, 31P
Pérez E., Márquez I., Marrero I., Durret F., González Delgado R. M., Masegosa J., Maza J., Moles M., 2000, A & A, 353, 893
Prieto M. A., Meisenheimer K., Marco O., Reunanen J., Contini M., Clenet Y., Davies R. I., Gratadour D., Henning T., Klaas U., Kotilainen J., Leinert C., Lutz D., Rouan D., Thatte N., 2004, ApJ, 614, 135
Rousset A., 1992, Ph.D. Thesis
Rozas M., Relaño M., Zurita A., Beckman J. E., 2002, A & A, 386, 42
Saripalli L., Mack K.-H., 2007, ArXiv Astrophysics e-prints
Sarzi M., Falcón-Barroso J., Davies R. L., Bacon R., Bureau M., Cappellari M., de Zeeuw P. T., Emsellem E., Fathi K., Krajnović D., Kuntschner H., McDermid R. M., Peletier R. F., 2006, MNRAS, 366, 1151
Sarzi M., Rix H.-W., Shields J. C., Rudnick G., McIntosh D. H., Ho L. C., Filippenko A. V., Sargent W. L. W., 2001, in Funes J. G., Corsini E. M., eds, ASP Conf. Ser. 230: Galaxy Disks and Disk Galaxies Supermassive Black Holes from the Survey of Nearby Nuclei with STIS. pp 261–262
Schinnerer E., Eckart A., Tacconi L. J., 2000, ApJ, 533, 826
Schinnerer E., Eckart A., Tacconi L. J., Genzel R., 2000, ApJ, 533, 850
Schmitt H. R., 2001, AJ, 122, 2243
Schoenmakers R. H. M., Franx M., de Zeeuw P. T., 1997, MNRAS, 292, 349
Shlosman I., Peletier R. F., Knapen J. H., 2000, ApJ, 535, L83
Sil'chenko O. K., Afanasiev V. L., 2004, AJ, 127, 2641
Simões Lopes R. D., Storchi-Bergmann T., de Fátima Saraiva M., Martini P., 2007, ApJ, 655, 718
Thornley M. D., Mundy L. G., 1997, ApJ, 484, 202
Tremaine S., Gebhardt K., Bender R., Bower G., Dressler A., Faber S. M., Filippenko A. V., Green R., Grillmair C., Ho L. C., Kormendy J., Lauer T. R., Magorrian J., Pinkney J., Richstone D., 2002, ApJ, 574, 740
Tully R. B., 1974, ApJS, 27, 437
Ulrich M.-H., 2000, A&A Rev., 10, 135
Ulvestad J. S., Ho L. C., 2001, ApJ, 558, 561
Vazdekis A., 1999, ApJ, 513, 224
Vila-Vilaro B., Robinson A., Perez E., Axon D. J., Baum S. A., Gonzalez-Delgado R. M., Pedlar A., Perez-Fournon I., Perry J. J., Tadhunter C. N., 1995, A & A, 302, 58
Wada K., 2004, in Ho L. C., ed., Coevolution of Black Holes and Galaxies Fueling Gas to the Central Region of Galaxies. pp 186–+
Wong T., Baitz L., Bosma A., 2004, ApJ, 605, 183
Wozniak H., Combes F., Emsellem E., Friedli D., 2003, A & A, 409, 469
Zhang X., Wright M., Alexander P., 1993, ApJ, 418, 100

APPENDIX A: NOTES ON INDIVIDUAL GALAXIES

A1 NGC 1068 (M 77)

NGC 1068 is one of the most nearby Seyfert 2 galaxies (D = 14.4 Mpc), and it has been well studied at different wavelengths. Ho et al. (1997) classified this active galaxy as a Seyfert of Type 1.8, but a dusty torus hides a Seyfert 1 nucleus (Antonucci & Miller 1985; Jourdain et al. 1994). NGC 1068's nucleus hosts a radio jet and an ionised cone at PA $\sim 10^\circ$ (Muxlow et al. 1996). Schinnerer et al. (2000) summarized the different observed morphological structures : the outer disk and the outer oval, the latter being interpreted as a primary bar, a HI ring at its Outer Lindblad Resonance and the two-arms inner spiral at its Inner Lindblad Resonance. A secondary Near-Infrared (NIR) bar extends up to about $16''$. The SAURON data we presented here have been already published by Emsellem et al. (2006), and we refer the reader to this paper for a detailed analysis: we here only provide a brief description of the revealed structures.

The stellar continuum map (Fig. 4a) shows elliptical isophotes, elongated along the PA of the NIR bar. The stellar velocity field (Fig. 4a) shows strong departures from axisymmetry, with an S-shaped zero velocity line, and a slightly varying orientation of the kinematics major-axis. The velocity dispersion rises towards the centre, reaching 200 $\mathrm{km\,s^{-1}}$ at R$\sim$10$''$and then presents a drop in the inner 5$''$with values down to about 100 $\mathrm{km\,s^{-1}}$. Gerssen et al. (2006) observed this galaxy with the Gemini Multi-Object Spectrograph (GMOS) IFU, covering the central 10×8 arcsec. Our stellar kinematics properties are in good agreement with theirs although they found a kinematic PA offset by about 13° from ours, their FOV being too small to detect the change of orientation of the kinematic major-axis.

Hβ and [O III] distributions are quite different (Fig. 4a). Hβ emission is very high in the inner 5$''$, and traces the spiral arms outside this region. As for Hβ , [O III] emission peaks in the central parts, with the distribution of [O III] becoming very asymmetric outwards. It is found predominantly in the North-East side, tracing the northern ionisation cone. Despite the significant differences between the distribution of the Hβ and [O III]line emission, their velocity fields and velocity dispersion maps are very similar (Figs. 4a and B1a). The velocity fields of Hβ and [O III] both display a prominent S-shaped zero velocity curve, evidence for strong deviations from circular motions. The velocity dispersion maps of Hβ and [O III] show a peak in the central 5$''$ parts and then reach lower values outside. As expected, the [O III]/Hβ is high in the region of ionisation cone ($\sim$ 10), and lower in the spiral arms ([O III]/Hβ $<$ 1), the latter being dominated by star formation regions (Figs. 4a).

A2 NGC 2655

NGC 2655 is an early-type spiral galaxy, hosting a Seyfert 2 nucleus. Optical and radio spectroscopic data exhibit off-plane gas in the central part (Erwin & Sparke 2003), and a dusty polar ring seen in Hα (Keel & Hummel 1988). This galaxy is interacting with its companion NGC 2715 and presents remnant signatures of a past merger (Huchtmeier & Richter 1982).

The stellar continuum map (Fig. 4b) shows an elongated feature, along the East-West direction, which corresponds well with the PA of the line of maximum stellar velocity. The stellar velocity field (Fig. 4b) is remarkably regular, with a PA around 90°. The velocity dispersion map shows a drop in the inner 3$''$.

Hβ and [O III] emission lines distribution and kinemat-

ics are similar (Figs. 4b and B1a). The emission lines are very bright in the inner 5″. Away from the centre, the distribution maps show a bright knot to the South-East side, 15″ away from the nucleus, and a lane at 10″on the West side: both features have been reported by Keel & Hummel (1988). The SE knot corresponds to high [O III]/Hβ ratio values ($\sim$ 4) similar to the ones obsered in the nuclear region. This feature could be driven by the radio jet (Keel & Hummel 1988). The emission lines ratio is smaller in the West lane (around 2-3). The emission lines velocity fields show strong departures from axisymmetry, with an S-shaped zero velocity curve, the kinematic major-axis having a changing PA, from $\sim 90^\circ$ in the inner 5″ to near 180° in the outer parts. As hinted by Sil'chenko & Afanasiev (2004), the ionised gas rotates together with the stars in the inner 5″, but follows the dust polar ring at radii $> 5'' - 6''$, rotating perpendicularly to the galactic plane. [O III] and Hβ velocity dispersion maps show the same features: a rise in the inner 5″ ($\sim$ 220 km s^{-1}) and in the western feature (305 km s^{-1}), and a roughly constant value outside (between 100 and 150 km s^{-1}).

A3 NGC 2985

NGC 2985 is an early-type spiral galaxy, with regular gas and stellar distributions. It is the control for NGC 4151. The disk orientation is determined by an inclination of $i = 40^\circ$ and a major-axis position angle of $PA = 180^\circ$. Noordermeer et al. (2005) report a tidal interaction with its companion NGC 3027.

The stellar velocity field of NGC 2985 shows a regular and symmetric pattern, consistent with motions in an axisymmetric gravitational potential (Fig. 4e). The PA of the kinematic major-axis (-2°) is aligned with the photometric major-axis of the outer disc. The velocity dispersion rises inwards, with 100 km s^{-1} at 15″from the centre and 150 km s^{-1} in the inner 5″. There is very little emission from the ionised gas Hβ and [O III] in NGC 2985 (Fig. 4e). The emission lines flux peaks in the inner 2″ with very little flux outside. The Hβ (Fig. B1b) and [O III] (Fig. 4e) kinematics are similar: the velocity fields are regular, showing the same overall symmetry as the stellar velocity field. The gaseous velocity dispersion maps show no specific features, with values rising towards the centre (200 km s^{-1} for [O III], 160 km s^{-1} for Hβ). Finally, the [O III]/Hβ line ratio reaches values up to 1.5-2 in the centre and decreases poutwards (for $r > 10$ ″).

A4 NGC 3227

NGC 3227 is a well studied barred galaxy, interacting with the elliptical galaxy NGC 3326, and with an associated dwarf galaxy (Mundell et al. 2004). The galactic disc has an inclination of 56°, with a outer photometric major-axis at a position angle $PA = 158^\circ$ (Mundell et al. 1995), coincident with the major-axis of the stellar bar. It is hosting a type 1.5 Seyfert nucleus (Ho et al. 1997). The central region has been mapped in ^{12}CO(1-0) and ^{12}CO(2-1) by Schinnerer et al. (2000), who detect molecular gas very close to the nucleus ($\sim$ 13 pc). The inner kpc regions host several complex features: a radio jet (PA $\sim -10^\circ$; Mundell et al. (1995)), an conical NLR outflow at a PA of about 15° (Mundell et al. 1995), an Hα outflow at PA $\sim 50^\circ$ (Arribas & Mediavilla 1994), and a molecular nuclear ring (Schinnerer et al. 2000).

Our SAURON stellar continuum map (Fig. 4a) presents an elongated structure (PA = 153°), aligned with the stellar bar. The stellar velocity field is regular (Fig. 4a), the major-axis being parallel to the galactic disc orientation. Outside $r > 5''$, the stars rotate rigidly (isovelocity contours parallel to each others). The stellar velocity dispersion rises towards the centre, reaching 200 km s^{-1} in the inner 5″.

Fig. 4a presents the [O III] and the narrow component of Hβ emission lines. The central broad component for the Hβ line corresponding to nuclear emission (BLR) has been removed. [O III] distribution is rather asymmetric, elongated on the North side of the field and Hβ emission lines extends from South-East to East. The [O III] and Hβ velocity fields are similar: they show strong deviations from axisymmetry with a PA of the major-axis changing from $\sim 30^\circ$ in the central regions, to about 170°, close to the stellar kinematic major-axis orientation. The velocity dispersion of both Hβ and [O III] rise towards the nucleus, reaching 310 km s^{-1} and 360 km s^{-1}, respectively in the centre. Finally, the [O III]/Hβ lines ratio map shows an elongated structure of high values (> 7) along the global kinematic major-axis (North-South).

A5 NGC 3351 (M 95)

NGC 3351 is a barred inactive spiral galaxy. It is the control object for NGC 4579. NGC 3351 hosts a large-scale stellar bar and an inner molecular bar-like feature in the centre (Devereux et al. 1992). The latter molecular structure is aligned with the major-axis of the galaxy (PA $\sim 10^\circ$) and perpendicular to the large scale bar. Two rings of HII regions associated with resonances due to the stellar bar exist: one inner ring with a radius of 10″ and another at 70″ from the centre. More recent observations in CO (Jogee et al. 2005) show evidence of the non-circular streaming motions in the inner region.

The SAURON stellar continuum map (Fig. 4f) shows a ring-like structure with $6'' \lesssim R \lesssim 10''$, which corresponds well with the HII ring at the presumed ILR of the large scale bar. The stellar velocity field is regular throughout the field of view. Stellar velocity dispersions are slightly lower (by $\sim$ 20 km s^{-1}) inside the ring than outside.

[O III] and Hβ distributions and kinematics do not differ much from each others. The intensity maps clearly show the known HII ring at $\sim 10''$ (Fig. 4f), and there is very little emission outside that structure. The gas velocity maps are regular, following the orientation observed in the stellar velocity field. The [O III] velocity dispersion map is almost featureless, with only a slight gradient from North-East (100 km s^{-1}) to South-West (140 km s^{-1}). There is a velocity dispersion drop ($\sim$ 50 km s^{-1}) for Hβ in the ring (Fig. B1b). The [O III]/Hβ lines ratio map show low values in the inner regions ($\lesssim 0.1$), as expected from star formation. [O III]/Hβ ratio is significantly higher outside the ring ($\sim$ 1), probably mostly due to the uncertainty in the emission line flux there.

A6 NGC 3627 (M 66)

NGC 3627 is an SAB spiral galaxy hosting a Seyfert 2 nucleus. It is part of the Leo Triplet system, interacting with

NGC 3623 and with evidence for a past interaction with NGC 3628 (Zhang et al. 1993). Previous radio and optical observations show asymmetric structures in the velocity field, non-circular gaseous motions and a molecular CO inner ring (Chemin et al. 2003). More recently, IFS data obtained by Afanasiev & Sil'chenko (2005) showed evidence for strong gaseous radial motions.

The SAURON stellar continuum map shows an elongated structure along the photometric PA $\sim 170°$ (Fig. 4c). The velocity field presents a regular rotation pattern, with a slight twist of the zero-velocity line in the very central parts ($r < 3''$). The stellar rotation follows the orientation of the photometric major-axis. The stellar velocity dispersion rises towards the central regions up to 120 $\mathrm{km\,s^{-1}}$.

The [O III] emission is concentrated in the inner $5''$, with some emission in an elongated structure, along the photometric PA (Fig. 4c). As for [O III], Hβ emission is preponderantly observed in the central parts, with an additional bright spot about $15''$ South of the nucleus. The [O III] and Hβ kinematics are quite similar (Figs. 4c and B1a). Their velocity fields show strong deviations from axisymmetry: the orientation of the kinematic major-axis changes from the external regions where it is aligned with the stellar kinematics, toward the nucleus where the ionised gas kinematic major-axis deviates by $\sim 40°$ from the stellar one. Afanasiev & Sil'chenko (2005) suggested that strong radial motions may exist in the central parts of this galaxy. Both [O III] and Hβ velocity dispersion maps are almost featureless, with a slight depression in the very centre. Finally, the [O III]]/Hβ lines ratio reaches its highest values in the inner $2''$.

A7 NGC 4051

NGC 4051 is an SAB galaxy classified as S1.2 by Ho et al. (1997). The stellar bar extends up to $\sim 50''$ along a PA $\approx 135°$. Radio-observations show a triple source at a PA $\sim 73°$ (Christopoulou et al. 1997), and the [O III] emission line distribution in the inner $3''$ is aligned with this radio component. The narrow-line profiles of NGC 4051 present strong blue wings. This blue-shifted component is also detected with SAURON in the Hβ and [O III] lines, and has therefore been fitted (see Sect. 2.4). Christopoulou et al. (1997) found evidence for a conical outflow, at $1\farcs5$ from the nucleus.

Our SAURON stellar continuum map (4d) show regular isophotes elongated along the PA of the large-scale bar. The stellar velocity field presents a regular and symmetric rotation pattern, the rotation axis being aligned with the photometric major-axis (PA$\sim 135°$). The stellar velocity dispersion decreases in the inner $5''$down to ~ 50 $\mathrm{km\,s^{-1}}$.

The emission line intensity is slightly extended towards the North-East, consistent with the ionised [O III] outflow cone observed by Christopoulou et al. (1997). The orientation of the ionised gas kinematic major-axis varies with radius: it is aligned with the stellar one in the outer part of the SAURON FOV, and then deviates by about $30°$ from the line-of-nodes of the galaxy. The Hβ emission line velocity dispersion reaches its highest values in the inner $5''$, while a decrease of dispersion is observed in these central regions for [O III]. The [O III]/Hβ lines ratio peaks at about $3''$ North-East from the nucleus, within the outflow region (Christopoulou et al. 1997).

A8 NGC 4151

NGC 4151 is one of the most well-studied galaxies of our sample. For a review on this galaxy and the AGN properties, see Ulrich (2000). It is an almost face-on barred spiral galaxy hosting a Seyfert type 1.5 active nucleus (Ho et al. 1997). The large-scale weak bar is elongated along a PA of about $130°$ and the photometric major-axis orientation is close to $20°$ (Mundell & Shone 1999). Its nuclear continuum and BLR emission are highly variable. It contains a radio jet along a PA of $77°$ and its Narrow Line Region (NLR) is extending over $\sim 10''$, and is aligned with the jet (Mundell et al. 2003).

Our stellar continuum map (Fig. 4e) presents rather round isophotes. The stellar velocity field shows a twist of the zero-velocity line in the inner $5\ ''$ which corresponds to the region where the BLR dominates the spectral features. A σ-drop is observed in the central part of the velocity dispersion map, but could be due to the BLR contamination. The [O III] and Hβ emission lines distributions are elongated on the South-West direction at a PA of about $50°$ associated with the NLR and the Extended NLR (ENLR, $R > 5''$ Asif et al. 2005). The emission lines ratio reaches very high values (~ 12) in this region. The ionised gas kinematics is dominated by rotation, but with some disturbances on the North-West side. [O III] emission line velocity dispersions peak in the inner few arcsec (~ 280 $\mathrm{km\,s^{-1}}$). Outside the very central parts, the velocity dispersion is between 50 and 130 $\mathrm{km\,s^{-1}}$. It increases at the edges of our map, corresponding to the location of a dusty ring (Vila-Vilaro et al. 1995). Asif et al. (1998) revealed the presence of streaming motions along this dust structure, which may be associated with the high [O III] velocity dispersion observed in our SAURON maps. Hβ velocity dispersion is flat in the outer parts ($R > 10''$, with σ between 80 and 130 $\mathrm{km\,s^{-1}}$) and rises regularly towards the center, reaching 200 $\mathrm{km\,s^{-1}}$ in the inner $3''$. The maximum velocity dispersion (~ 350 $\mathrm{km\,s^{-1}}$) is reached at about $3\farcs5$ North-East of the centre.

A9 NGC 4459

This S0 galaxy is in the Virgo cluster. It is the control non-active galaxy for NGC 2655. The SAURON data presented here (Fig. 4b) are part of the SAURON project (de Zeeuw et al. 2002) and were therefore already published elsewhere (Emsellem et al. 2004; Sarzi et al. 2006).

The stellar component of NGC 4459 shows roundish isophotes, and its stellar velocity field presents a very regular rotation pattern the major-axis of which is parallel to the line-of-nodes (PA $\sim 77°$). The velocity dispersion rises towards the centre, reaching 200 $\mathrm{km\,s^{-1}}$ (Fig. 4b). There is almost no ionised gas emission (our maps have been clipped at 3σ), except for the very centre ($R < 3''$).The emission lines velocity field seems to be dominated by rotation, and the velocity dispersion rises from about 80 $\mathrm{km\,s^{-1}}$ for $R > 3''$ to 160 $\mathrm{km\,s^{-1}}$ for Hβ (200 $\mathrm{km\,s^{-1}}$ for [O III]) inside $3''$. The [O III]/Hβ line ratio rises regularly towards the centre.

A10 NGC 4579 (M 58)

NGC 4579 is an active galaxy classified as S1.9/L1.9 (Ho et al. 1997). It hosts a NIR stellar bar of 9 kpc of diameter,

oriented along PA = 58°. García-Burillo et al. (2005) observed this galaxy with the Plateau de Bure Interferometer (CO) as part of the NUGA survey. They found a nuclear molecular spiral from $R \sim 1$ kpc down to ~ 200 pc, driven by the stellar bar and detected highly non-circular motions over the spiral arms. They interpreted these perturbations as outflow motions.

Fig. 4f presents our SAURON maps for this galaxy. The stellar continuum isophotes are rather round in the centre and slightly elongated along a PA of $\sim 60°$ corresponding to the orientation of the stellar bar. The stellar velocity field presents a very regular rotation pattern, with a kinematic major-axis oriented at a PA of 95°. The stellar velocity dispersion rises regularly towards the centre.

[O III] and Hβ distribution and kinematics are very similar (Figs. 4f and B1b). The ionised gas intensity maps show a spiral-like structure which corresponds to the nuclear molecular structure observed by García-Burillo et al. (2005). The [O III]/Hβ ratio presents lower values in the spiral arms than outside. The ionised gas kinematics is complex and shows strong departures from axisymmetry. The gas kinematic major-axis ($PA = 100°$) is almost perpendicular to the stellar bar, and varies within the SAURON field of view. Despite the similarities between Hβ and [O III] distributions and velocity fields, their velocity dispersions are significantly different. The $\sigma_{[OIII]}$ map presents an elongated structure of high values along the stellar bar (Fig. 4f), while $\sigma_{\mathrm{H}\beta}$ decreases in the central parts Fig. B1b.

A11 NGC 5055 (M 63)

NGC 5055 is a spiral non-active galaxy, control for NGC 5194. Previous radio and optical studies show an overall remarkable regularity and symmetry in its morphology and kinematics (Thornley & Mundy 1997; Battaglia et al. 2006). There are evidence for a tidal interaction with a companion (UGC 8313), and the outer disk of NGC 5055 is warped. Blais-Ouellette et al. (2004) studied the Hα emission of NGC 5055 with a Fabry-Perot: they found two velocity components in the inner 8″of this galaxy. One component is consistent with the global disk kinematics while the second one exhibits a pattern compatible with a bipolar outflow or a counter-rotating disk.

Our SAURON stellar continuum map presents an asymmetry towards the North-West (Fig. 4g). The stellar velocity field shows very regular rotation pattern with the kinematic major-axis aligned with the photometric one at a PA of 100°. The velocity dispersion rises in the very centre ($r < 2''$).

The ionised gas Hβ and [O III] are mainly concentrated in the inner 5″. The [O III] distribution shows a V-shaped structure towards the North, while the Hβ intensity map shows a number of hot spots broadly distributed over the FOV. The [O III] and Hβ velocity fields are very regular and similar to the stellar velocity field (except for their higher amplitudes). [O III] velocity dispersion maps is featureless but Hβ velocity dispersion map shows an elongated structure of high dispersion roughly aligned with the kinematic major-axis. Finally, the [O III]/Hβ lines ratio reaches its highest values in the region of high [O III] emission line flux.

A12 NGC 5194 (M 51)

NGC 5194 is an almost face-on spiral galaxy in interaction with NGC 5195. Its nucleus is classified as a Seyfert type 2 (Ho et al. 1997). Many studies have been made on the structure and the nucleus of this nearby galaxy. A large outflow bubble extents up to $\sim 9''$ (~ 42 pc) North of the nucleus and a bright cloud is located about 3″South of the nucleus. These structures have been observed at different wavelengths (Ford et al. 1985), and they are found to trace the biconical NLR along a PA of 163°. NGC 5194 is hosting a radio-jet which interacts with the surrounding interstellar medium.

The SAURON stellar continuum map (Fig. 4f) shows the presence of dust lanes. The stellar velocity field has a regular rotation pattern with its major-axis at a PA $\sim -165°$, deviating by $\sim 25°$ from the presumed line of nodes orientations (PA = 170°, Tully 1974). The stellar velocity dispersion is featureless.

Hβ emission line flux is very high in the centre and for $R > 5''$ it traces the spiral arms of the galaxy. The [O III] emission line flux traces the ionisation cone of NGC 5194. The [O III] intensity map shows the outflow bubble in the North and the bright cloud in the South of the nucleus corresponding to the end of the radio-jet. The emission line ration [O III]/Hβ peaks in the centre (with values up to 8) and in the southern cloud (values between 3 and 5). The ionised gas velocity field seems to be dominated by simple galactic rotation, but presents some distortions very probably due to the outflow observed in the inner 10″. The ionised gas velocity dispersion rises towards the centre.

A13 NGC 5248

NGC 5248 is a nearby inactive spiral galaxy, control for both NGC 4051 and NGC 6951. It harbours two prominent circum-nuclear rings (Laine et al. 2001) and an inner molecular spiral within 1.5 kpc driven by the large scale bar (Jogee et al. 2002). The arms of the spiral connect with the inner circumnuclear ring. Jogee et al. (2002) also mention the presence of streaming motions in this galaxy.

The stellar continuum shows an elongated structure along the global disk orientation at $PA \sim 150°$ (Fig. 4d). The velocity field presents a regular rotation pattern, the major-axis of which is oriented at a PA of 115°, aligned with the photometric major-axis ($PA = 105$ deg Jogee et al. 2002). A σ-drop is revealed by our velocity dispersion map in the inner 3″with an amplitude of ~ 60 km s^{-1}.

The Hβ emission line distribution shows a ring-like structure with a radius of $\sim 5''$. The [O III] distribution is concentrated within the central few arcseconds, and in the two brightest peaks of the ring. This ring-like structure corresponds to the known ring of HII region described by Laine et al. (2001). The [O III]/Hβ emission line ratio is lower inside the ring (0.15), consistently with the presence of star formation, and rises slightly towards the very centre (0.7). The ionised gas velocity field is dominated by rotation with its major-axis aligned with the stellar kinematic one. The Hβ velocity dispersion map shows a depression in the star formation ring (50 km s^{-1}), and slightly rises towards the very centre (80 km s^{-1}, Fig. B1b). The [O III] velocity disper-

sion map shows not specific features, with roughly constant values around 50 $\mathrm{km\,s^{-1}}$.

A14 NGC 5806

This non-active galaxy is the control for NGC 3627. Carollo et al. (2002) observed this galaxy with the HST/NICMOS2 camera in the near-infrared. They detect a prominent bulge and a stellar bar structure in the circumnuclear regions. They classified NGC 5806 as a galaxy with a concentrated nuclear star formation mixed with dust. Our SAURON data is presented in Figs. 4c, B1b and . The stellar morphology and kinematics are quite regular. The stellar continuum within the SAURON field of view is elongated along the outer photometric major-axis of the galaxy (PA = 170°). The stellar velocity field shows a regular rotation pattern with the kinematic-major axis aligned with the photometric major-axis. The velocity dispersion is rising toward the nucleus reaching about 120 $\mathrm{km\,s^{-1}}$ in the centre.

The [O III] and Hβ emission line distribution show elongated features along the photometric PA. That feature exhibits a ring-like structure in Hβ, broken in the North-East part, at a radius $\sim 3''$. The [O III]/Hβ ratio shows rather low values in the Hβring (~ 0.3), consistent with star formation. The gas velocity maps are dominated by rotation, and resemble the stellar velocity field, though with a higher amplitude. The ionised gas velocity dispersion maps show no particular structures.

A15 NGC 6951

NGC 6951 is a spiral galaxy which has a large stellar bar (PA $\sim 90°$). Its nucleus is classified as Seyfert 2 (Ho et al. 1997), but Pérez et al. (2000) suggest that it could be considered as a transition object, between a very high excitation LINER and a Seyfert 2. The ionised gas (Hα) is mainly concentrated in the nuclear region and form an annulus of radius $\sim 5''$, in which massive star formation is taking place. Pérez et al. (2000) interpreted the Hα kinematics in the circumnuclear zone as a series of nested disks, decoupled from one another.

The stellar continuum presents isophotes elongated along a PA consistent with the galactic disk major-axis Rozas et al. (PA$\sim$ 138° 2002). The stellar velocity field shows regular rotation pattern whit the major-axis aligned with the line-of-nodes of the galaxy. The stellar velocity dispersion shows a drop in the inner $5''$.

The Hβ emission line distribution map shows a inner broken ring elongated along the major-axis of the galaxy ($PA = 137°$) while [O III] is dominated by the AGN contribution, its intensity maps showing a compact central peak in the inner $3''$, with no particular feature outside. The emission line ratio [O III]/Hβ reaches very low values in the ring (0.2), consistent with the presence of on-going star formation in the annulus, and rises towards the centre (values of up to 6) where the effect of the AGN is prominent. The velocity fields are quite regular, dominated by the global rotation, and aligned with the stellar kinematics. The emission line velocity dispersion rises rapidly towards the centre reaching about 100 $\mathrm{km\,s^{-1}}$ close to the nucleus for both the Hβ and [O III] emission lines. These values are in good agreement with those found by Pérez et al. (2000).

APPENDIX B: Hβ KINEMATIC MAPS

In this section we present the Hβ kinematic maps for each galaxy.

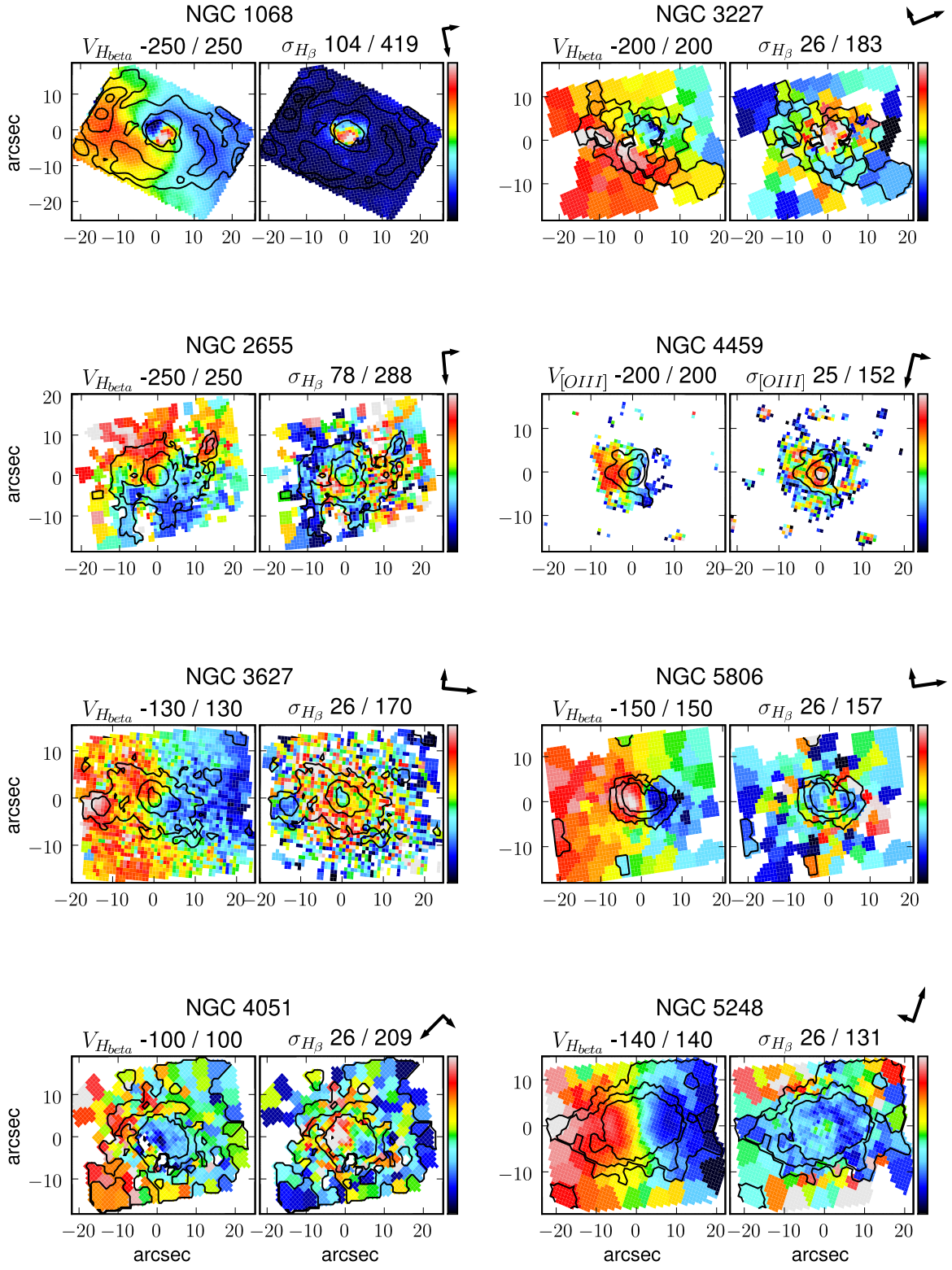


Figure B1a. Velocity and velocity dispersion of Hβ emission lines. Each row present a pair : Seyfert on the left, Control on the right, except for NGC 1068 and NGC 3227 which are shown together in the first row. For NGC 4459, the [O III] velocity and velocity dispersion maps are shown (see Sec. 3. All the maps are orientated so that the photometric major-axis of the galaxy is on the x-axis. The units are in km s^{-1}. The color scale is shown on the right hand side and the cut levels are indicated in the top right corner of each map. The long and short arrows on the right of each galaxy name show the North and the East directions, respectively.

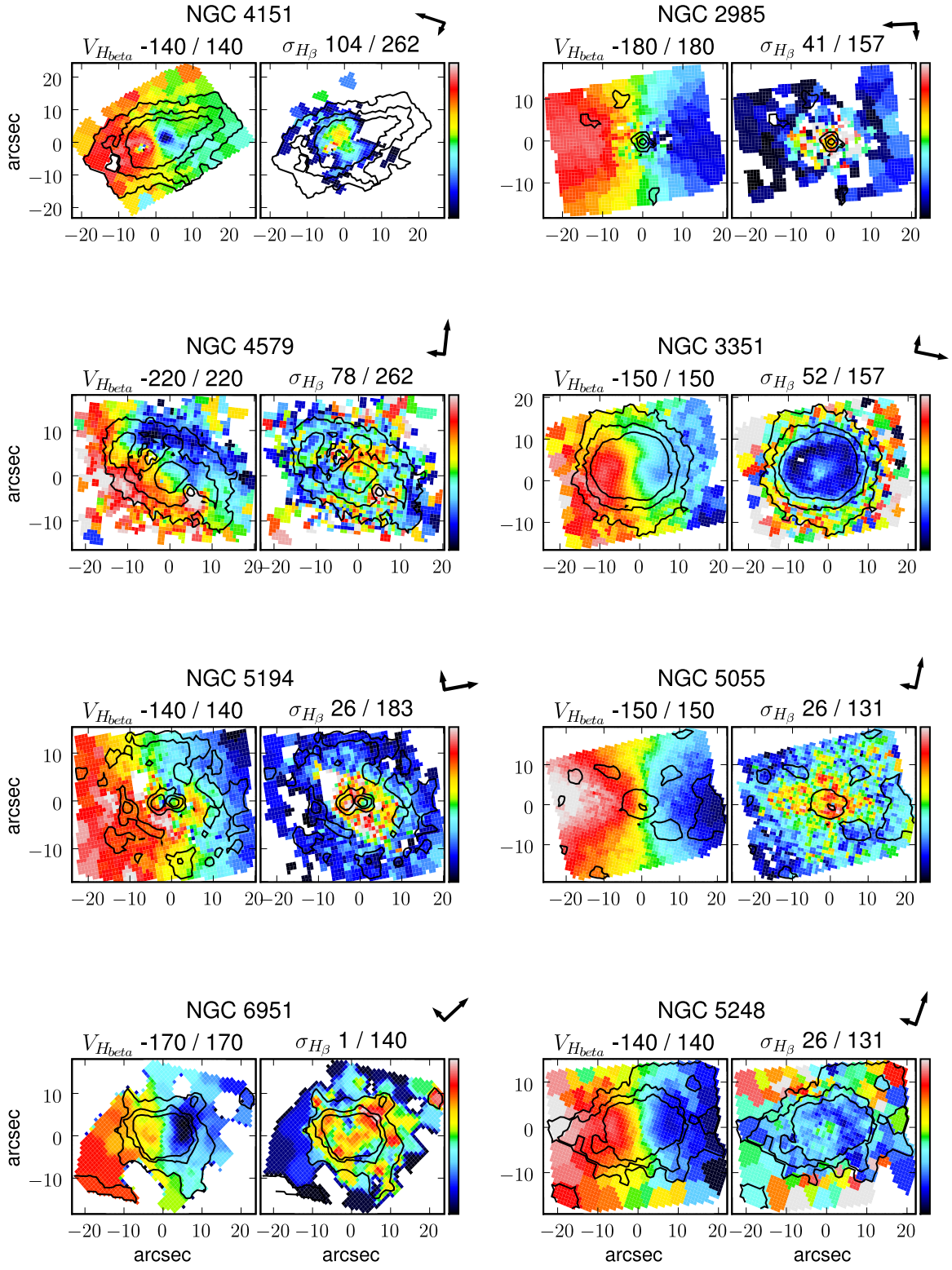


Figure B1b. Fig. B1a continued.